Integrated Master in Bioengineering
Specialization in Biological Engineering

Studies of Interphase Formation between Biomolecules and Metal and Oxide Surfaces in Aqueous Environment

Marta Pereira Pinheiro

Master thesis carried out at

Fraunhofer Institute for
Manufacturing Technology and Advanced Materials IFAM

Supervisor at FEUP: Prof. Dr. Maria do Carmo Pereira

Supervisor at IFAM: Dr. Klaus Rischka

September 2017

ACKNOWLEDGMENTS

I would like to thank everybody in the Department of Adhesives and Polymer Chemistry at Fraunhofer IFAM, who have always made me feel welcome, and whose kindness and helpfulness have turned this time at IFAM into such a smooth and enjoyable journey. I am very grateful to my supervisor Dr. Klaus Rischka, without whom this dissertation would not be possible. Thank you for providing me the opportunity to realize my master thesis in your group. I would like to express my gratitude to my supervisor at FEUP (LEPABE), Prof. Dr. Maria do Carmo Pereira, for her valuable advices and for the review of this thesis.

A very special thanks to Linda Gätjen for her continuous support and motivational remarks. Thank you for all the patience, valuable suggestions and crucial support. I would like to voice my sincere gratitude to Dr. Michael Noeske for sharing so much of his precious time with very important investigations for the development of this work. Thank you for all the inspiring conversations and for sharing your knowledge and extensive expertise with me. I would like to thank Dr. Dirk Salz, Dr. Karsten Thiel and Amelie Greif for their kind contributions with very important performed experiments. Thank you!

Nada disto seria possível sem o apoio da minha querida família e amigos. Obrigada Cici, Tinho, princesa da Pérsia e avó, por nunca me deixarem sem-abrigo ou esfomeada pelo Porto. Muito obrigada à minha família do coração, Pessoa, Tats e Gina, por todos esses dias e noites de amizade e carinho infinitos. Às minhas migas de sempre, Sara, Joana, Maria e Rebeca, por estarem presentes desde que tenho memória. Sofia, por todas as apresentações imaculadamente formatadas, máscaras faciais e tostas francesas, e por todos os beijinhos que não me deste, estão cá dentro. Querida Catarina, por todas as memórias que cruzam a Rua da Saudade, especialmente em direção à pastelaria após noites cansadas. Ao meu amigo Júnio Zeferino, porque se um desejo me fosse concedido estaríamos de volta a esses tempos loucos no Vagon para celebrar isto, mas a vida não é suficientemente justa para permitir tal coisa. Ao Philipp, por todas as horas diariamente partilhadas, obrigada por continuares a sobreviver de forma exímia. Obrigada!

Esta tese é dedicada aos meus pais e irmão, por todo carinho e apoio incansáveis, e por serem o melhor exemplo que poderia ter.

ABSTRACT

Non-covalent functionalization is frequently required in graphene-based materials. Interfactants are characterized by irreversibly adsorbing to solid surfaces. Self-assembly of biomolecules exhibiting an interfactant-like behavior may emerge as a route for controlling thin films growth comprising graphene oxide (GO) monolayers in aqueous environment. In this work, two enzymes (laccase from *Trametes versicolor* and lysozyme from hen egg white) and a polypeptide (Poly-L-lysine) were tested upon directing GO layer formation on silicon dioxide (SiO_2) and titanium oxide (TiO_2) solid surfaces. Layer-by-layer assembly of biomolecules and GO was investigated by quartz crystal microbalance with dissipation monitoring (QCM-D), X-ray photoelectron spectroscopy and scanning electron microscopy. Antimicrobial and biocompatible properties of analogous titanium-coated surfaces were assessed.

Tested interfactants showed higher adsorption on TiO_2 rather than on SiO_2 and under pH conditions close to their isoelectric points (IEP). Among the tested biomolecules, PLL was indicated as the most promising interfactant for directing GO layer formation on the tested surfaces. Adsorption of PLL and GO on the studied interfaces tended to be influenced by both pH and substrate. GO adsorption onto a pre-coated PLL surface was higher under pH 6.1, bellow the IEP of PLL. Biomolecules tended to form rigid thin films on the solid substrates, while its adsorption on GO-coated surfaces revealed formation of a viscoelastic growing material. Titanium surfaces ere coated with PLL followed by GO and the obtained surfaces revealed no antimicrobial activity against *Escherichia coli* (*E. coli*), in which the GO average sheet size was over 10 µm. Nevertheless, equivalent coated titanium surfaces showed remarkable biocompatibility after 24h of direct contact with mouse connective tissue fibroblasts (cell line L929). The percentage of viable cells after contact with the GO-coated surfaces was approximately 93 ± 2% of the untreated control.

Keywords: graphene oxide, biomolecules, layer-by-layer assembly, molecular interactions, QCM-D

RESUMO

A funcionalização não covalente é frequentemente requerida em materiais à base de grafeno. Moléculas interfactantes são caracterizadas por adsorver irreversivelmente em superfícies sólidas. A auto-montagem de biomoléculas que apresentam um comportamento típico interfactante pode emergir como forma de promover o crescimento controlado de filmes finos incorporando monocamadas de óxido de grafeno (GO) em meio aquoso. Neste trabalho, duas enzimas (lacase de *Trametes versicolor* e lisozima de clara de ovo de galinha) e um polipéptido (poli-L-lisina) foram testados para dirigir a formação de camadas de GO em superfícies sólidas de dióxido de silício (SiO_2) e óxido de titânio (TiO_2). A montagem camada-por-camada de biomoléculas e GO foi analisada utilizando uma microbalança de cristal de quartzo com monitoração de dissipação (QCM-D), espectroscopia fotoeletrónica de raios X e microscopia eletrónica de varrimento. Foram avaliadas as propriedades antimicrobianas e de biocompatibilidade de superfícies análogas de titânio revestidas.

Os interfactantes testados demonstraram maior adsorção em TiO_2 do que em SiO_2 em condições de pH próximas dos seus pontos isoelétricos (IEP). Entre as biomoléculas testadas, PLL foi indicada como o interfactante mais promissor para dirigir a formação de camadas de GO nas superfícies de teste. A adsorção de PLL e GO nas interfaces em estudo tenderam a ser influenciadas pela variação de pH e substrato. A adsorção de GO numa superfície pré-revestida por PLL foi superior a pH 6.1, abaixo do IEP do poliaminoácido. As biomoléculas tenderam a formar filmes rígidos quando adsorvidas diretamente nos substratos, enquanto a sua adsorção em superfícies pré-revestidas por GO revelou a formação de material com características viscoelásticas. Superfícies de titânio foram revestidas com PLL seguida de GO e as superfícies obtidas não revelaram atividade antimicrobiana contra *Escherichia coli* (*E. coli*), nas quais o tamanho médio das folhas de GO era superior a 10 µm. No entanto, superfícies de titânio equivalentes demonstraram notável biocompatibilidade após 24 h de contacto direto com fibroblastos do tecido conjuntivo do rato (linha celular L929). A percentagem de células viáveis depois de contacto com as superfícies revestidas por GO foi aproximadamente 93 ± 2% do controlo não tratado.

Palavras Chave: óxido de grafeno, biomoléculas, montagem camada-por-camada, interações moleculares, QCM-D

DECLARATION

I hereby declare that I am the sole author of my thesis and that no other sources than those listed have been used. Furthermore, I declare that I have acknowledged the work of others by providing detailed references of said work. I hereby also declare that my thesis has not been prepared for another examination or written assignment, either wholly or excerpts thereof.

Place, date	*Signature*

TABLE OF CONTENTS

List of Terminology

Symbols

ΔD	dissipation variation
Δf	frequency variation
-COOH	carboxyl
D	dissipation
f	frequency
n	overtone number
$-NH_2$	amine
-OH	hydroxyl
v/v	volume per volume
w/v	weight per volume
w/w	weight per weight

Units of Measurement

°C	degrees Celsius
µL	microliter
µm	micrometer
h, min	hours, minutes
Hz	hertz
M	moles per liter
mm, nm	millimeter, nanometer
ng/cm^2	nano gram per square centimeter

Abbreviations

2D	two-dimensional
at.%	atomic percent
BSA	bovine serum albumin
CCC	critical coagulation concentration
CMC	critical micelle concentration
CNTs	carbon nanotubes
DU	dissipation units (1E+6), dimensionless factor in terms of dissipation
DXR	doxorubicin hydrochloride
e.g.	*exempli gratia* (latin for ’for example’)
et al.	*et alii* (latin for ‘and others’)
etc.	*et cetera* (latin for ‘and other things’)

FLG	few-layer graphene
GO	graphene oxide
i.e.	*id est* (latin for ’that is’ or ’that means’)
IEP	isoelectric point
IS	ionic strength
LAC	laccase
LEPABE	Laboratório de Engenharia de Processos, Ambiente, Biotecnologia e Energia
LB	Lauria Bertani Broath
LbL	layer-by-layer
LYS	lysozyme
PLL	poly-l-lysine
PVD	physical vapor deposition
QCM-D	quartz crystal microbalance with dissipation monitoring
rGO	reduced graphene oxide
SDS	sodium dodecyl sulfate

List of Figures

List of Tables

CHAPTER 1

Introduction

Understanding the factors that influence the interaction between biomolecules and abiotic surfaces is of most interest in diverse fields with applications ranging from biosensing, biocatalysis and biomedical research to nanoscale electronics, hybrid functional materials or even environmental technology. Several proteins and polypeptides have been identified as specific binders to many abiotic surfaces, such as metal and oxide surfaces and, more recently, graphene materials.

Graphene consists of a micrometer-sized molecule in which carbon atoms participate in robust covalent bonds between sp^2 hybridized states forming an extended honeycomb topology. Since its discovery in 2004, graphene has been extensively studied due to its intrinsic chemical and physical properties. Graphene oxide (GO) is part of the graphene family materials and differs from graphene by the addition of oxygen atoms bound with the carbon scaffold, which makes GO hydrophilic and easily dispersible in water. GO modified through covalent bonds has been studied for a number of different applications in the last years. More recently, many approaches have been focusing on non-covalent functionalization of GO, which tends to lead to enhanced dispersibility, biocompatibility, binding capacity or sensing properties.

Immobilization of biomolecules in a multilayer system through layer-by-layer (LbL) deposition allows constructing thin films with nanometer control over the film thickness, which in turn provides highly defined control over the physicochemical interaction with the surrounding environment. QCM-D is a remarkable technique for facilitating investigations into the LbL assembly process. It is an acoustical method that allows monitoring the adsorption of molecules onto the surface of quartz crystal resonators and at the same time provides information about the structural properties of the adsorbed materials.

Predicting and analyzing adsorbed monolayers of biomolecules and GO on solid surfaces raises substantial experimental and theoretical challenges, considering the structural complexity of the involved molecules. Proteins and polypeptides may act as interfactant molecules which differ from surfactants due to the irreversible character of their adsorption to solid surfaces. The aim of this work comprised assessment of potential different biomolecules upon directing GO layer formation on SiO_2 and TiO_2 solid surfaces by QCM-D. Obtained results were compared to X-ray photoelectron spectroscopy (XPS) investigations of analogous coated surfaces. Additionally, antimicrobial and biocompatible properties of these coatings on a commercial titanium substrate were tested. GO has been indicated as a promising material for the development of antimicrobial surfaces which also makes it a potential candidate for biological and biomedical applications. However, the relationship between GO physicochemical properties and its antimicrobial activity, as well its biocompatibility and toxicity to biological systems, have yet to be elucidated.

CHAPTER 2

State of The Art

2.1 Graphene Family Materials: Physicochemical Properties and Applications

In 1947 graphene was studied in theory by P.R. Wallace as a textbook example for calculations in solid state physics at the National Research Council of Canada (Wallace, 1947), having predicted the electronic structure of the nanomaterial. Furthermore, R.S. Ruoff and co-workers (1999) suggested a process for graphene extraction through a mechanical exfoliation method in order to extract thin layers of graphite from a graphite crystal. However, it was not possible to observe any monolayers.

Graphene was isolated in 2004 (Novoselov *et al.*, 2004) for the first time and since then it has been extensively studied owing to its extraordinary physicochemical and structural properties. K. Geim and K.S. Novoselov from the University of Manchester, UK, were awarded with the Nobel Prize in Physics 2010 for "groundbreaking experiments regarding the tow-dimensional material graphene" (The Nobel Prize in Physics, 2010). The material has already demonstrated excellent electrical properties (*e.g.*, high carried mobility and capacity), electrochemical properties (*e.g.*, high electron transfer rate), optical properties (*e.g.*, excellent ability to quench fluorescence), structural properties (*e.g.*, one-atom thickness and high surface-to-volume ratio) and mechanical properties (*e.g.*, robustness and flexibility) (Liu *et al.*, 2012). Thus, graphene has become an incredibly fast-growing nanomaterial in industry with applications ranging from optoelectronic and high-energy physics to material science, biomedicine, as well as environmental applications (Bharech and Kumar, 2015).

Graphene is a single atom-thick sheet of sp^2-bonded carbon atoms arranged in a 2D honeycombed lattice which is considered the basic building block of many carbon allotropes (Abergel *et al.*, 2010). The International Editorial Team of Carbon (Hurt, 2013) recommended a nomenclature for the 2D carbon materials where the monolayer is the purest known form of graphene. It is also possible to define few-layer graphene (FLG) which are a small number (two to ten) of well-defined, countable, graphene layers, and depending on the number of layers they exhibit different properties. GO is the oxidized form of graphene, consisting of a monolayer with high oxygen content, where a typical O/C atomic ratio can be a value around 0.58 (Haubner *et al.*, 2010). Reduced graphene oxide (rGO) is obtained from GO which is reductively processed to remove the oxygen-containing groups. Graphene nanomaterials are defined as 2D graphene materials with a lateral dimension up to 100 nanometers (nm) which include graphene nanosheets, graphene nanoribbons, graphene nanoflakes, graphene nanoplatelets, *etc*. Fig. 1 shows some of the different graphene family materials.

The oxidation of graphite using strong oxidizing agents introduces oxygenated functionalities in the graphite structure which not only expand the layer separation, but also makes the material hydrophilic. These oxidized layers can be exfoliated in water under ultrasonication, originating the above-mentioned GO

(Novoselov *et al.*, 2004). Compared with graphene, GO possesses two important characteristics to be mentioned: firstly, it can be produced with inexpensive graphite as raw material by cost-effective chemical methods, and secondly, it is highly hydrophilic, forming stable aqueous colloids to facilitate the assembly of macroscopic structures (Pei and Cheng, 2012). Nowadays, GO is prepared mostly by the modified Hummers methods. According to this method, graphite is oxidized to graphite oxide by treatment with water-free mixture of concentrated sulfuric acid, sodium nitrate and potassium permanganate (Hummers and Offman, 1958).

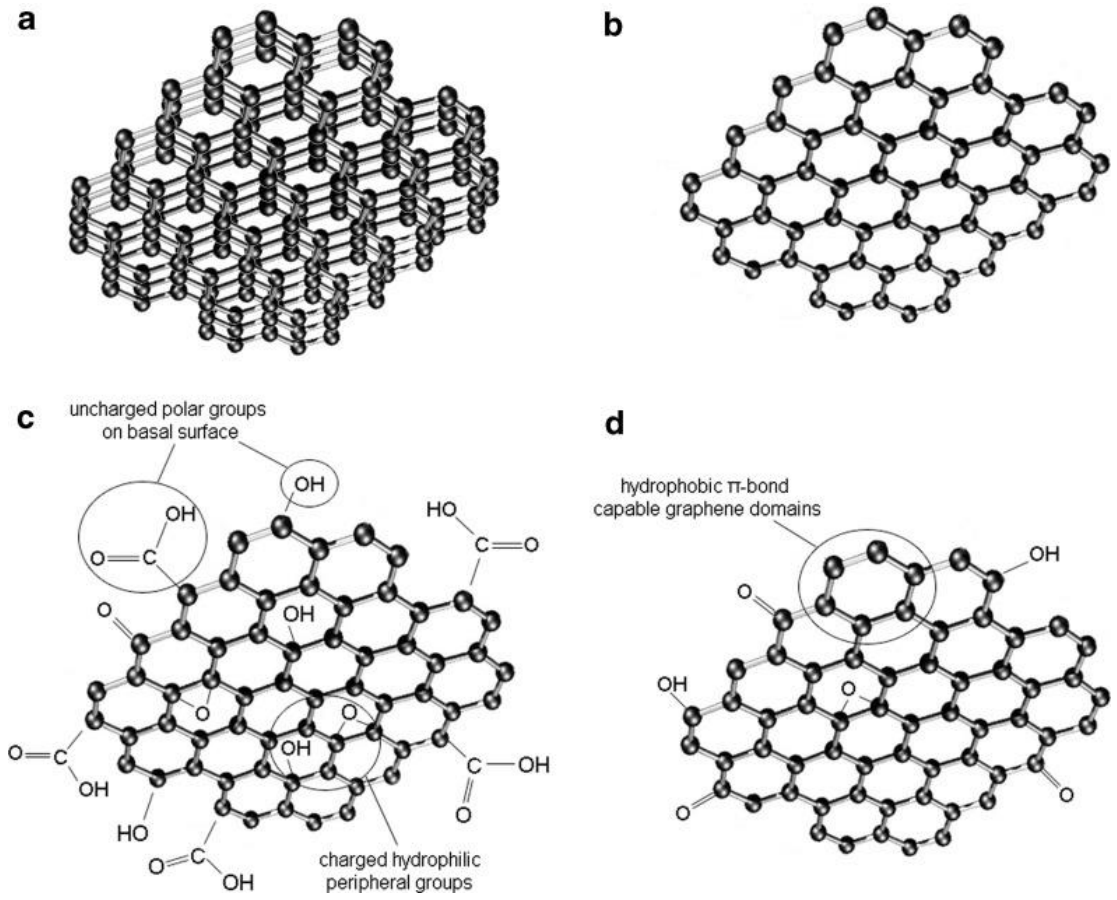

Figure 1. Graphene family materials.
(a) few-layer graphene, (b) graphene nanosheet, (c) graphene oxide, (d) reduced graphene oxide. (Adapted from Jastrzębska *et al*., 2012).

The chemical structure of GO is still not clear since its partial amorphous character increases its complexity. However, the widely accepted model is the Lerf-Klinowski model (Klinowski *et al*., 1998), where the carbon basal planes are decorated with epoxy and hydroxyl functional groups, in addition to carbonyl and carboxyl groups along the edges. Due to the presence of most of its functionalities on the edges, this area of GO is hydrophilic whereas the basal plane, even being decorated with some functional groups, possesses mostly a hydrophobic character. The result of this combination is an amphiphilic micrometer-sized molecule (Simsikova and Sikola, 2017). From the previously mentioned fact arises one

of the advantages for GO applications, namely its easy dispersability in water and other organic solvents due to the presence of the oxygen-containing groups.

A strong characteristic of the graphene sheets is its perfectly flat arrangement of trigonally bonded sp^2 carbon atoms. On the other hand, GO sheets are also partly arranged with tetrahedrally bonded sp^3 carbon atoms, being displaced slightly above or below the graphene plane. However, even considering this structure deformation and presence of functional groups, graphene-like honeycomb lattice in GO is preserved (Pandey *et al*., 2008). Thus, GO can be described as a random distribution of oxidized regions combined with non-oxidized areas, where carbon atoms have sp^2 hybridization preserved (Pei and Cheng, 2012). Since conductivity of graphene is mostly related to the long-range conjugated network of the hexagonal graphitic lattice, the covalent character of C–O bonds on GO disrupts the original sp^2 conjugation, modifying the electronic structure and making it an insulator (Zhao *et al*., 2010). Nevertheless, recovery of electrical conductivity can be partially achieved by reduction of GO, giving place to rGO. While chemical reduction of GO is currently seen as the most suitable method of mass production of graphene, it has been difficult to complete the task of producing graphene sheets of high quality on a large scale. Once this issue is overcome, one can expect to see graphene become much more widely used in commercial and industrial applications. On the other hand, functionalization of GO can fundamentally change its properties, and the resulting chemically modified graphene can be suitable for a number of applications (Georgakilas *et al*., 2016).

The above-mentioned unique structural and physicochemical features of graphene-based materials have motivated explorations into its wide potential applications. For example, on the development of new electrochemical sensors, use of graphene has been reported for successful detection of nucleic acids (Lou *et al*., 2012), protein biomarkers (Kumar *et al*., 2014), differentiated biomolecules such as dopamine (Mao *et al*., 2015), or even for the detection of environmental contaminants such as catechol (Palanisamy *et al.*, 2017). Graphene-based materials have also been developed as gas sensors (Yang *et al*. 2016). Different approaches have also been made on biomedical fields, namely for tissue engineering (Dubey *et al.*, 2015), drug delivery (Zhang *et al*., 2017) and bioimaging (Kundu *et al.*, 2017).

Graphene, in particularly GO, has been extensively proposed as an effective antibacterial agent. Recently, Nanda *et al.* (2016) have studied the antibacterial mode of action of GO against *Escherichia coli* (*E. coli*) and *Enterococcus faecalis* using Raman spectroscopy. Moreover, graphene-based materials have also been applied for environmental applications, namely for water purification by removal of aromatic pollutants (Yang *et al*., 2015) and membranes preparation for water desalination (Surwade *et al*., 2015).

2.2 Noncovalent Functionalization of Graphene Oxide

Functionalization is the best way to achieve the best performance out of graphene materials. In literature, one will find application of graphene materials modified through both covalent bound (Karousis *et al.*, 2011; Xu *et al.*, 2009) and noncovalent interactions (Ureña *et al.*, 2017; Yu *et al.*, 2017).

GO can be functionalized with porphyrins through the formation of amide bonds between amine-functionalized porphyrins and carboxylic groups of GO. Xu and co-workers (2009) showed that the covalent interaction between porphyrin and GO surface results in an improvement in the dispersibility in organic solvents and an effective fluorescence quenching after the photoexcitation of the porphyrin. Nevertheless, noncovalent functionalization is generally preferred since it allows introduction of new chemical groups without compromising graphene structural properties (Georgakilas *et al*., 2016), and at the same time avoiding the effect of aggressive chemicals and high temperatures. Moreover, noncovalent functionalization has a nonpermanent character which improves the flexibility of the final products.

As explained in the previous section, GO contains both aromatic (*i.e.*, sp^2 hybridized) and aliphatic (*i.e.*, sp^3 hybridized) domains, which expands the type of interactions that can occur at the surface. Concerning GO interaction with other molecules, since it is a micrometer-sized molecule, it is several magnitudes larger than the participating section of the modifying molecules. Consequently, there should be considered multiple interactions on both sides of GO sheets (Georgakilas *et al*., 2016).

Regarding noncovalent functionalization of GO, van der Waals forces are one type of interaction to be considered. Usually, these interactions involve GO sheets and organic molecules or polymers with high hydrophobic character (Georgakilas *et al*., 2016). GO has also been reported to stablish hydrophobic interactions due to the hydrophobic character of its basal plane (Pires *et al*., 2014).

Graphene is a π-system, being characterized by its perfect aromatic surface. Noncovalent intermolecular interactions involving π-systems are critical to the stabilization of biomolecules like proteins or functional nanomaterials (Georgakilas *et al*., 2012). Although aromatic regions on GO sheets are smaller when compared with a graphene sheet, it is important to consider that some π-interactions may likely occur. This type of interaction is promoted when the interacting molecule also possesses a π-system. The strength of interaction is dependent on the number of aromatic rings of the interacting molecule and on the planarity of the two components (*i.e.*, GO and interacting molecule), since the interaction requires an overlap between them (Gao, 2012). To give an example, Lu and co-workers (2009) produced a hybrid material of GO and doxorubicin hydrochloride (DXR) prepared via noncovalent interactions, having suggested that π-π interactions and hydrophobic interactions are on the origin of the interaction between DXR and sp^2 networks of GO.

In addition, other types of interactions arise from the presence of oxygen functionalities on GO surface and edges, namely hydrogen bonds and electrostatic interactions. On the previous-mentioned study, Lu and co-workers (2009) have reported a strong hydrogen bonding between hydroxyl (-OH) and carboxyl (-COOH) groups of GO and -OH and amine ($-NH_2$) groups of DXR. Moreover, Simsikova (2016) studied the interaction between GO and different albumins, having predicted an interaction of electrostatic and hydrophobic character.

Some studies have been showing that different types of interactions determine a different orientation of the modifying molecules both on graphene and GO surfaces. For instance, it has been demonstrated that

aromatic molecules tend to lie parallel to the graphene and GO basal plane (Georgakilas *et al*., 2016), while both hydrogen bonds and hydrophobic interactions promote a stand upright arrangement of the molecules on the surface (Coletti *et al*., 2010).

Noncovalent Functionalizing Agents of Graphene Oxide: Functionalization with Biomolecules

Several types of functionalizing agents have been studied for noncovalent functionalization of graphene materials. These may include functionalization with polymers, therapeutic drugs, carbon nanoallotropes, nanoparticles, biomolecules, *etc.* In this sub-section, some examples of different types of functionalization will be presented, with particular attention to the functionalization of GO with biomolecules.

Many studies have been demonstrating successful incorporation of graphene nanostructures into polymer matrixes though noncovalent interaction. A repeating aromatic polymer unit can strongly interact with graphene monolayers, due to the existence of π-π interactions between them, resulting in polymer composites with improved mechanical, electrical and thermal properties (Chandra and Kim, 2011; Stankovich *et al*., 2006). On the other hand, polymers without a π-system have also been reinforced with graphene or GO. Matos *et al.* (2014) reported the use of cetyltrimethylammonium bromide, a cationic surfactant, to disperse GO or rGO into natural rubber. A polymer composite was obtained with enhanced chemical, electrical and mechanical properties.

Graphene materials have been studied as platforms for the stabilization and delivery of therapeutic drugs. In drug delivery, applied graphene nanostructures must be hydrophilic, allowing facile dispersion of the produced material in water and biological fluids (Georgakilas *et al*., 2016). Thus, owing its hydrophilic character, GO may be applied to make more water soluble some important therapeutic drugs. For instance, hypocrellins are highly active pigments toward many kinds of tumor cells, but their use *in vitro* is very limited due to its poor water solubility. Zhou and co-workers (2012) showed that hypocrellins can be made more soluble in water when interacting with GO. In their study, hypocrellin B was loaded on GO and the interactions between them were attributed mainly to π- π interactions and hydrogen bonds.

Carbon nanotubes (CNTs) are a carbon nanoallotrope with a strong aromatic character that allows them to establish π-π interactions with graphene materials, such as graphene or GO. This combination has been successfully applied for the production of nanoarchitectured aerogels, foams, membranes, *etc.* (Georgakilas *et al.*, 2015). GO has also been used for the production of stable dispersions of pristine CNTs in water. Tang and co-workers (2014) demonstrated the production of conductive carbon polymer composites where interaction between carbon nanotubes and GO (*i.e.*, hydrophilic GO sheets) is exploited to disperse conductive but non-polar CNTs and form a stable colloidal solution.

Graphene materials have been studied as substrates for nanoparticles where graphene properties, such as high surface area, conductivity and binding sites, can be beneficial. Several studies have been reporting GO interaction with nanoparticles for many applications, such as nanostructures for catalytic

applications (Tiwari *et al*., 2013), nanostructures for lithium-ion batteries (Li *et al*., 2013) or magnetic nanostructures for wastewater treatment (Chandra *et al*., 2010).

Graphene materials have been combined with biomolecules in a variety of different applications on biomedical, sensing and environmental fields. Noncovalent interactions have been used to attach proteins, peptides, nucleic acids, cells and bacteria to GO. For instance, Guo *et al*. (2011) showed that interaction between GO and herceptin, a monoclonal antibody used to treat breast cancer, leads to a conjugate exhibiting constant fluorescent intensity, making it a potential bio-probe for live cell imaging. Zhang and co-workers (2010) explored the catalytic activity of GO immobilized horseradish peroxidase (HRP) for removal of several phenolic compounds from industrial wastewater. A higher removal efficiency of the complex GO-HRP in comparison to soluble HRP was verified.

Protein immobilization is an efficient way to make its biotechnological processes more favorable, providing cost effectiveness and better stability of the biomolecule under both storage and operational conditions (Mohamad *et al.*, 2015). A substantial part of GO bio-applications is based on molecular interaction between GO and proteins. Therefore, it is very important to understand how GO and proteins interact with each other. However, although recent studies have already reached some important findings, the whole understanding of the interaction mechanism between GO and proteins is still representing a challenge.

Noncovalent protein adsorption on solid surfaces represents the most desirable strategy of physical immobilization (Simsikova and Sikola, 2017). Protein adsorption on GO can include noncovalent interactions such as van der Waals forces, hydrogen bonds, electrostatic, hydrophobic and π-π interactions. Usually, these types of functionalization involve solution phase incubation of the two components, followed by a rinsing step to remove the remaining unbound proteins (Palanisamy *et al.*, 2017; Zhang *et al.*, 2010).

Interaction between proteins and GO is dependent on the charge of the functional groups of the protein, which in turn is strongly dependent on the environmental conditions (*e.g.*, pH value, ionic strength of the medium). Therefore, considering its isoelectric point (IEP), a determined protein can have a zero, positive or negative net charge depending on the surrounding conditions. Surface density of oxygen-containing groups on GO may also vary depending on the preparation procedure and storage conditions (Simsikova and Sikola, 2017). Thus, potential electrostatic interactions between proteins and negatively charged GO may be limited by these conditions.

Also van der Waals forces can drive GO interaction with proteins. However, electrostatic interactions have been reported as more pronounced on GO interactions with other molecules, whereas van der Waals forces are more related to interactions between proteins on rGO. This seems to be verified due to decrease of oxygen-containing groups on the rGO surface (Baweja *et al.*, 2015).

On the other hand, since GO basal plane has some sp^2 hybridized areas preserved, physical adsorption of proteins can also be mediated by hydrophobic interactions where hydrophobic regions of the protein interact with the carbon lattice of GO basal plane (Simsikova, 2016). Moreover, enrichment of the

basal plane with some aromatic regions allows GO to interact with proteins through π-π interactions. Alwarappan and co-workers (2012) reported strong π-π interactions between GO basal plane and aromatic residues of glucose oxidase, when studying the electrochemical biosensing performance of single-, few- and multilayered GO for detection of glucose.

In conclusion, protein immobilization on GO surface tends to be a synergic combination of different types of interactions, where several attractive and repulsive interactions and the effective driving force that determines a specific binding are different for various classes of proteins (Simsikova and Sikola, 2017).

2.4 Layer-by-Layer Assembly of Biomolecules and Graphene Oxide

Self-assembly processes rely on the formation of selected structures through spontaneous association of atoms, molecules, clusters and particles. Taking into account that noncovalent interface functionalization is frequency required in graphene-based approaches, biomolecular self-assembly has emerged as a route for creating diverse and well-defined surface chemistry at graphene interfaces (Ariga *et al.*, 2014).

LbL assembly is a highly versatile method for fabrication of controlled layered structures of different component materials (*e.g.*, polymers, colloids, biomolecules, cells) using simple and inexpensive procedures. It is based on the sequential construction of thin films with nanometer control over film thickness, which also allows defined control over physicochemical properties of the nanostructured materials (Richardson *et al.*, 2016). Traditionally, LbL assembly for planar substrates is performed by simply immersing the substrate in the polymer solution or colloidal suspension, where the adsorption onto the surface is promoted by diffusion-driven kinetics. This process is followed by a rinsing step in order to wash off the unbounded molecules (Ariga *et al.*, 2014).

Stamboroski and co-workers (2016) have recently suggested the term polymeric interfactant layer for polymeric monolayers formed by polypeptides or proteins on various solid substrates. Polymeric interfactant films may be considered 2D layers with molecular dimensions in which each molecule spans between the substrate below it and the neighboring phase above it (Ureña *et al.*, 2017). Ureña and co-workers (2017) studied adsorption of GO from aqueous dispersions on aluminum oxide surfaces previously modified with an interfactant layer of a chemically non-reactive polymer. Polymeric interfactants were reported as molecules that strongly attach to a wide range of substrate surfaces and may play a fundamental role upon directing GO layer formation.

When aiming at studying deposition of nanoarchictectured films comprising biomolecules and GO on solid surfaces, prediction and analysis of adsorbed monolayers at such interfaces represents a substantial experimental and theoretical challenge. Considering a polypeptide or protein which adsorbs to a solid surface, one face is exposed to the substrate (*i.e.*, important for adsorption stability) and the other face is exposed to the solvent. The face which is exposed to the solvent will be important for different phenomena such as analyte binding, solubilization, or coupling to create extended materials (Russell and Claridge, 2016). In the last case, an option might be adsorption of GO on the pre-existing molecular monolayer on

the substrate, creating a peptide interface with GO. This last GO layer might be followed by another peptide layer, following a LbL assembly of biomolecules as GO. Taking into account that noncovalent adsorption depends on a delicate balance of molecule-substrate, molecule-molecule, and molecule-solvent interactions (MacLeod and Rosei 2014), a single peptide can have many binding modes. In this specific case of LbL assembly of a peptide on a solid surface followed by GO, one may consider the different binding modes for peptide on a determined substrate; for GO on the peptide monolayer; and for peptide on the GO monolayer.

Assembly of thin films requires assessing if the layer materials are deposited as intended, quantification of the growth process, as well as characterization of film morphology, internal film structure, film mechanical and thermal properties (Richardson *et al.*, 2016). Different techniques can be applied for deposition of thin films on planar substrates depending on the substrate and properties of the thin films to be examined. Regarding assessment of film growth, QCM-D has become one of the most widely used methods (Ureña[1] *et al.*, 2016; Yu *et al.*, 2017), allowing evaluation of LbL assembly by measuring the changes in frequency and dissipation of a quartz crystal resonator. This technique will be analyzed in more detail in the following section.

2.5 Quartz Cristal Microbalance with Dissipation Monitoring for the Study of Thin Films Comprising Biomolecules and Graphene Oxide

QCM-D is an acoustical method that will be the focus of this study for analysis of interaction between different biomolecules and GO when deposited as thin film layers on oxide surfaces. The method is sensitive to mass coupling and viscoelastic changes occurring close to the quartz crystal sensor surface (Ureña[1] *et al.*, 2016). In this section, the principle of QCM-D will be shortly presented and some examples of its application for the analysis of peptide-graphene interfaces will be mentioned.

In 1880, Jacques and Pierre Curie demonstrated the so-called *piezoelectric effect*. They discovered that when a mechanical stress is applied to some materials such as quartz, a voltage proportional to the stress is produced (Curie and Curie, 1880). Later, Sauerbrey (1959) discovered that quartz oscillation frequency depends on the change in the surface mass. Thus arose the term quartz crystal microbalance (QCM), leading to the use of quartz resonators as sensitive microbalances for thin films. When voltage is applied to a quartz crystal, it oscillates at a specific frequency and the mass on the quartz surface is directly related to the change in frequency of the oscillating crystal. Sauerbrey equation (Equation 1) was described as follows:

$$\Delta f = -\frac{2f_0^2}{\sqrt{\rho_0 \mu_0}} \frac{\Delta m}{n}$$

(Equation 1)

where Δf is the measured frequency change (Hz), f_0 is the resonance frequency (Hz), ρ_0 is the density of the quartz crystal ($2.648\ \mathrm{g/cm^3}$), μ_0 is the shear modulus of the quartz crystal ($2.947 \times 10^{11}\ \mathrm{g/cm\ s^2}$), Δm is the mass change (g) and n is the overtone number (Vashist and Vashist, 2011). Overtones are the acoustic

waves of greater frequency than the fundamental frequency accompanying a sound with a defined tone pitch (*e.g.*, 3rd overtone consists of oscillations in three sections) (Ardley, 2003). The change in QCM frequency determines the mass of analyte adsorbed in ng/cm^2. The Sauerbrey equation is only valid when the deposited films are homogeneously distributed, the adsorbed films are rigid and the overall adsorbed mass is less than 2% of the sensor mass (Vashist and Vashist, 2011).

In contrast to a rigid film, the loaded mass on the crystal might have viscoelastic properties that will influence the damping of the oscillation, defined as dissipation factor (*D*). Once ΔD is considered significant, changes of the resonant frequency can no longer be considered equivalent to changes in adsorbed mass and mathematical models are required to quantify the changes to the add layer on the surrounding fluid. The dissipation factor is the sum of all energy losses in the system per oscillation cycle (BiolinScientific[1], 2017). As a viscoelastic ('soft') film does not fully couple to the oscillating crystal, the Sauerbrey equation will underestimate the adsorbed mass. QCM-D takes into account both frequency and dissipation of the quartz crystal, where *D* is defined by Equation 2 as follows:

$$D = \frac{E_{Lost}}{2\pi E_{Estored}} \qquad \text{(Equation 2)}$$

where E_{Lost} is the energy lost during one oscillation cycle and $E_{Estored}$ is the total energy stored in the oscillator. When molecules adsorb to the oscillating crystal, water couples to the adsorbed material as an additional dynamic mass and the layer is sensed as a viscoelastic 'hydrogel' (BiolinScientific[1], 2017). Fig. 2 shows how the frequency and dissipation of the oscillating quartz crystal behave when a rigid or viscoelastic molecule adsorbs on the crystal surface.

Considering its above-mentioned advantages, QCM-D has been extensively reported as a powerful surface technique for studying interactions between biomolecules and surfaces (Cai *et al.*, 2015; Chandrasekaran *et al.*, 2013). On the other hand, only a few studies have been focusing on the conjugation between peptides and graphene oxide studied by QCM-D.

Chowdhury and co-workers (2014) studied the deposition and release of GO using QCM-D. They evaluated the influence of different mono- and divalent salts on the deposition and release of GO on PLL coated silica surfaces. GO deposition was found to decrease at high ionic strengths (IS) due to aggregation, which reduced the diffusion coefficient of GO and consequently reduced the deposition rate on the surface. This phenomenon was verified above a determined critical coagulation concentration (CCC) for each studied salt. Regarding the release of deposited GO, the fraction of GO released decreased with increasing IS. This was attributed to the reduced energy barrier from increasing IS and higher attractive forces between GO flakes, as predicted by Derjaguin-Landau-Verwey-Overbeek (DLVO) theory.

Cai and co-workers (2015) developed modified gold surfaces with a bovine serum albumin (BSA) conjugated GO. They studied red blood cell adhesion and hemolysis using QCM-D and could demonstrate

an excellent hemocompatibility of the BSA modified GO. The modified surface decreased red blood cell adhesion under flow conditions, maintained the cells morphology and reduced the hemolysis rate in comparison with the pristine gold surface. Therefore, the hemocompatibility of the bio-functionalized GO could confer its potential for biomedical applications.

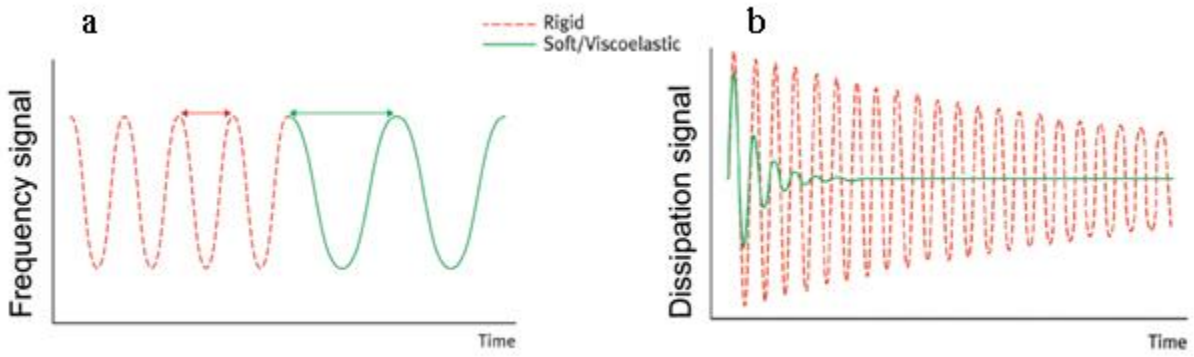

Figure 2. QCM-D response upon adsorption of rigid or viscoelastic materials.
(a) Changes in the frequency of the oscillating sensor crystal when the mass is increased by addition of a rigid and viscoelastic molecular layer; (b) Difference in dissipation signal generated by a rigid and 'soft' molecular layer on the sensor crystal. (Adapted from BiolinScientific[1], 2017).

Lastly, Frost *et al.* (2016) investigated size dependency of GO sheets on its interaction with lipid membranes, and how it varies between small and large liposomes. They explored the LbL assembly of these materials by combination of QCM-D and indirect nanoplasmonic sensing (INPS). Interesting results were obtained, for instance, spontaneous liposome rupture onto GO was observed for large lateral dimensions of the GO sheets. Furthermore, it was possible to interleave not only lipid membranes but also liposomes between GO sheets with large lateral dimensions. The obtained results may allow a better control over LbL assembly of the studied materials.

CHAPTER 3

Materials and Methods

This chapter is organized in two differentiated parts. The first part describes the used materials, which include chemicals, equipment, test surfaces and used software. The second part consists on the description of the applied methods, including graphene oxide purification, contact angle measurements, QCM-D, XPS and scanning electron microscopy (SEM). Finally, preparation of coated surfaces for XPS and SEM analysis, antimicrobial and biocompatibility tests are described.

3.1 Materials

The used materials are presented in the following tables. Unless otherwise specified, chemicals were used as received without further purification.

3.1.1 Chemicals

The used chemicals and respective providers are presented in Table 1.

Table 1. Chemicals specification and respective providers.

Chemical	Company/Provider
Graphene oxide Graphene oxide water dispersion, 4 mg/mL, monolayer content > 95%	Graphenea (San Sebastián, Spain)
Laccase Laccase C from *Trametes versicolor*, > 1 U/mg	ASA Spezialenzyme GmbH (Wolfenbüttel, Germany)
Lysozyme Lysozyme from Hen Egg White, 120000 U/mg	Sigma-Aldrich Chemie GmbH (Steinheim, Germany)
Poly-L-Lysine Poly-L-Lysine Hydrochloride, molecular weight 15-30 kDa	Sigma-Aldrich Chemie GmbH (Steinheim, Germany)
Acetic Acid $C_2H_4O_2$ > 99.7%	Sigma-Aldrich Chemie GmbH (Steinheim, Germany)
Sodium Acetate $C_2H_3NaO_2$ > 99%, water free	Carl Roth GmbH (Karlsruhe, Germany)
2-(N-morpholino)ethanesulfonic acid MES Hydrate, > 99.5% (titration)	Sigma-Aldrich Chemie GmbH (Steinheim, Germany)
Hellmanex® II Liquid cleaning concentrate, for glass, quartz cells and optical components	Helma GmbH & Co. KG (Müllheim, Germany)

Continuation of Table 1. Chemicals specification and providing company.

Sodium dodecyl sulphate $C_{12}H_{25}NaO_4S$ ≥ 98.5%	Sigma-Aldrich Chemie GmbH (Steinheim, Germany)
Hexadecyltrimethylammonium bromide $C_{19}H_{42}BrN$ ≥ 99%	Sigma-Aldrich Chemie GmbH (Steinheim, Germany)
Hydrogen peroxide solution H_2O_2 30% (w/w) in H_2O, contains stabilizer	Sigma-Aldrich Chemie GmbH (Steinheim, Germany)
Ammonia solution NH_4OH 25% (v/v) in H_2O, for analysis EMSURE®	Merck KG aA (Darmstadt, Germany)
HPLC grade water	Across Organics (Geel, Belgium)

3.1.2 Equipment

The used equipment and respective providers are presented in Table 2.

Table 2. Equipment specification and respective providers.

Instrument	Provider
UV/Ozonisator UV/Ozone ProCleaner™	BioForce Nanosciences, Inc. (Ames, Iowa, USA)
Quartz crystal microbalance with dissipation monitoring QCM-D E4	Q-Sense (Gothenburg, Sweden)
Peristaltic pump IPC-N 4	ISMATEC® (Wertheim, Germany)
Centrifuge Megafuge 16R	Thermo Fisher Scientific
Ultrasonic Bath Sonorex RK 100	Bandelin Electronic GmbH & Co KG (Berlin, Germany)
pH Meter S20 SevenEasy™ pH	Mattler Toledo (Hamburg, Germany)
Ultrapure water system Arium® pro	Sartorius AG (Göttingen, Germany)
Goniometer OCA15 Plus	DataPhysics Instruments GmbH (Filderstadt, Germany)

3.1.4 Test Surfaces

The origin of the used test sample surfaces are described in the following sub-sections.

Silicon dioxide-coated and titanium-coated QCM-D sensors

The silicon dioxide-coated quartz crystal sensors (SiO_2 sensors) (QSX 303, LOT-QuantumDesign GmbH, Darmstadt, Germany) and the titanium-coated quartz crystal sensors (Ti sensors) (QSX 310, LOT-QuantumDesign GmbH, Darmstadt, Germany) were supplied optically polished with a surface roughness of the electrode less than 1 nm (RMS). The sensor has 14 mm of diameter, 0.3 mm of thickness and an electrode layer of 40 nm.

Plasma coated silicon oxide and titanium dioxide surfaces

Plasma coated silicon dioxide (SiO_2) and titanium oxide (TiO_2) surfaces were gently prepared by Dr. Dirk Salz. SiO_2- and TiO_2-based thin film coatings were applied to the surface of silicon (Si) wafer substrates using low pressure plasma enhanced chemical vapor deposition (PECVD) technique. The home built low pressure plasma chamber was equipped with a TRUMPF Hüttinger Quinto system for radio frequency (13.56 MHz) generation. More detailed information about the coating process is specified elsewhere in Stamboroski *et al.*, 2016.

Titanium (Ti) surfaces

Titanium 6Al4V ELI, 20 x 20 x 1 mm^3, was obtained from ARA-T Advance (Dinslaken, Germany).

3.1.5 Software

The used software for data acquirement and analysis is listed in Table 3.

Table 3. Used software and respective provider.

Software	Provider
QSoft 401 Version 2.5	Biolin Scientific (Västra Frölunda, Sweden)
QTools Version 3.0	Biolin Scientific (Västra Frölunda, Sweden)
Q-Sense Dfind Version 0.35	Biolin Scientific (Västra Frölunda, Sweden)
SCAN 20	DataPhysics Instruments GmbH (Filderstadt, Germany)

3.2 Methods and Characterization

This section describes the applied methods in the present study. Both antimicrobial activity and biocompatible tests were performed under sterile conditions.

3.2.1 Purification of Graphene Oxide

The commercial GO dispersion (4 mg/mL) was purified before use as follows: 1 mL of the commercial GO solution was added to an Eppendorf and centrifuged for 3 minutes (min). The supernatant was discharged and the pellet was dispersed in 1 mL of ultrapure water using vortex and ultrasound. The procedure was repeated five times and the last pellet was dispersed in ultrapure water. The suspension was used to prepare formulations containing 25 µg/mL GO in the used buffers.

3.2.2 Buffers Preparation

The used buffers were prepared with ultrapure water and are listed in Table 4. Its preparation is described in the in the following sub-sections.

Acetate buffer preparation

A stock solution of 200 mM acetic acid was prepared by diluting 11.78 mL of acetic acid to 1000 mL of ultrapure water. Afterwards, a second stock solution of 200 mM sodium acetate was prepared by diluting 16.57 g sodium acetate to 1000 mL of ultrapure water. 250 mL of 200 mM acetic acid was titrated with 200 mM sodium acetate to the desired pH of 4.7. The same procedure was followed with titration to the desired pH of 3.6. It yield two 200 mM sodium acetate buffer solutions of 4.7 ± 0.2 and 3.60 ± 0.2 at 25 °C (appendix C-1).

MES buffer preparation

1.47 g of MES was diluted in 150 mL of ultrapure water. The solution was titrated with 10 M NaOH to the desired pH of 6.1, 9.0 and 11.0. The final volume was adjusted to 250 mL. It yielded three 30 mM MES buffer solutions of 6.1 ± 0.2 and 9.0 ± 0.2 and 11.0 ± 0.2 at 25 °C (appendix C-1).

Table 4. Used buffers, respective concentrations and pHs.

Buffer	Concentration (mM)	pH
Sodium Acetate Buffer	200	3.6
Sodium Acetate Buffer	200	4.7
MES	30	6.1
MES	30	9.0
MES	30	11.0

3.2.3 Contact Angle Measurements

The contact angle is the angle at which a liquid/vapor interface meets the solid surface. Contact goniometry is a method to determine the wettability of a surface, which depends on the surface tensions of the involved interfaces such that the total energy is minimized. The degree of wetting is described by the contact angle (Förch *et al.*, 2009). If the liquid is very strongly attracted to the solid surface, the droplet will completely spread out on the solid surface and the contact angle will be close to zero degrees. Less strongly hydrophilic solids will have a contact angle up to 90°. If the solid surface is hydrophobic, the contact angle will be larger than 90° (Förch *et al.*, 2009).

The contact angle of a liquid drop on a solid surface is defined by the mechanical equilibrium of the drop under the action of the solid/vapor (γ_{SV}), solid/liquid (γ_{SL}), and liquid/vapor (γ_{LV}) interfacial energies (Fig. 3). This equilibrium relation is known as Young's equation (Young, 1805), which assumes a perfectly flat surface and can be written as:

$$0 = \gamma_{SV} - \gamma_{SL} - \gamma_{LV} \cos\theta \qquad \text{(Equation 3)}$$

Where θ is the contact angle and γ_{SV}, γ_{SL}, and γ_{LV} represent the interfacial energy at the solid/vapor, solid/liquid and liquid/vapor interface, respectively.

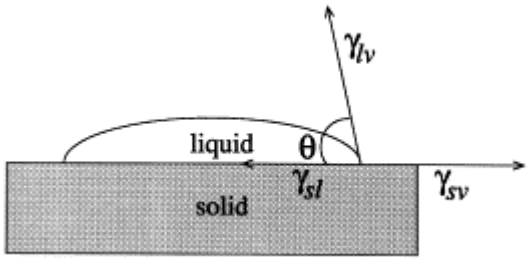

Figure 3. Schematic of a sessile-drop contact angle system. (Kwok and Neumann, 1999).

The apparent contact angles of the naked test surfaces were measured with a goniometer (OAC15 Plus, Data Physics Instruments, Filderstadt, Germany) using the sessile drop technique. HPLC grade water (Across Organics) was used as probe liquid and a drop of 10 µL was used for each measurement. The reported contact angles were an average of three different measurements on different surface areas. The recorded images were analyzed using SCAN 20 data Physics software.

3.2.4 QCM-D Measurements

Quartz Crystal Microbalance with Dissipation Monitoring

Experiments were carried out under flow conditions using a quartz crystal microbalance with dissipation monitoring (QCM-D) with four flow modules and a chamber volume of 40 µL each (E4, Q-Sense,

Gothenburg, Sweden) (Fig. 4). SiO_2- and Ti-coated quartz crystals were used, operating at a fundamental frequency of 5 MHz and its 3rd, 5th, 7th, 9th, 11th and 13th overtones.

QCM-D experiments were performed to evaluate the adsorption of different materials on SiO_2 and Ti sensors in two different sets of measurements described in the following sub-sections. For all measurements, changes in frequency (*f*) and dissipation (*D*) were monitored in real time at 25 °C. The *f* is given in Hz, while the dissipation factor *D* is dimensionless since it is a ratio of energies, being reported as 10^{-6} dissipation units (DU). Sensors were mounted in the respective QCM-D flow modules (Fig. 4) which were connected to a peristaltic pump (IPC, ISMATEC, Wertheim, Germany) by tubes, providing a homogeneous flow of 100 µL/min through the module under hydrostatic pressure. The system was equilibrated with buffer for at least 10 min in order to generate a stable baseline before each measurement.

Changes in *f* and *D* were recorded with QSoft 401 (BiolinScientific, Sweden). The resulting data was extracted with QTools (BiolinScientific, Sweden) for *f* and *D* plot as a function of time. Q-Sense Dfind (BiolinScientific, Sweden) was used for modeling data according to either a rigid (Sauerbrey relation) or viscoelastic (Smart Fit) model. The used software allows modeling of the obtain *f* and *D* data to a specific model with a defined model fit given as percentage (%), which is a value that helps the user choosing a model that describes data the best. This model will estimate adsorbed mass (ng/cm^2) and thickness (nm) variation of the formed films. The 5th overtone was used to interpret the produced data in this study. This selection was made according to the overtone that showed more stability (*i.e.*, lower background noise) over all the performed experiments.

Figure 4. QCM-D E4.
System with four flow modules in a temperature controlled chamber. The flow module on the right side is open, showing a gold-coated quartz crystal for placement into the flow module. (BiolinScientific[2], 2017).

QCM-D Preparation

Before each experiment, the used quartz crystal surfaces were treated with UV/ozone (UV/Ozone ProCleaner™, BioForce Nanosciences, USA) for 10 minutes. Then, the crystal was placed into the flow module as indicated by Fig. 5. The modules were connected through the tubes to the peristaltic pump and inserted into the QCM-D chamber. At this point, the pump could be started and the flow modules filled with buffer solution. The generator was digitally controlled using the QSoft 401 software and a constant temperature was adjusted. Before starting data acquisition, the desired overtones were chosen and the resonance frequencies of each sensor were searched. The peaks for each resonance frequency were displayed and they must be as narrow as possible without a fronting or tailing, avoiding poor signals that could indicate a broken sensor or a sensor that was not well positioned into the module.

Figure 5. Flow module by Q-Sense.
QCM-D flow module with a quartz crystal sensor placed in the flow chamber. (BiolinScientific[3], 2017).

QCM-D Cleaning

The flow modules, tubes and quartz crystal surfaces were cleaned according to the 'Cleaning & Immobilization Protocols' by Q-Sense (Q-Sense, 2008) with some changes due to the use of GO. After each measurement, 1% (v/v) Hellmanex®II in ultrapure water was pumped through the system at 40 °C with a flow rate of 200 µL/min for 15 min. When GO was pumped through the system during an experiment, 1% (v/v) Hellmanex®II solution was also left overnight in the system at room temperature. Afterwards, ultrapure water was pumped through the system at 40 °C with a flow rate of 500 µL/min for 30 min. The flow modules and tubes were dried with nitrogen gas.

SiO_2- and Ti-coated quartz crystal sensors were cleaned with two different protocols (Q-Sense, 2008). For cleaning SiO_2-coated quartz crystal sensors (QSX 303), the sensor surfaces are treated with UV/ozone for 10 min. Then, the sensors are immersed in a solution of 2% (w/v) SDS in ultrapure water for 30 min at room temperature and rinsed with ultrapure water. Finally, the sensors are dried with nitrogen gas and treated with UV/ozone for 10 min. For cleaning Ti-coated quartz crystal sensors (QSX 310), the sensor surfaces are immersed in 1% (v/v) Hellmanex®II solution for 30 min at room temperature, rinsed with

ultrapure water and dried with nitrogen gas. Finally, the sensors are sonicated in 99% ethanol for 10 min, rinsed with ultrapure water, dried with nitrogen gas and treated with UV/ozone for 10 min.

The complete flow modules were opened and cleaned every two weeks to avoid contamination due to remaining organic material. Six screws were removed from the flow module which was then divided in two metal parts. These two metal parts together with the sealing gasket and the O-ring (Fig. 6) were immersed in 2% (w/v) SDS solution and sonicate for 30 min while heating to 40 °C. Finally, they were rinsed with ultrapure water and dried with nitrogen gas.

Figure 6. Different parts of the flow module disassembled for cleaning. (Q-Sense, 2008).

QCM-D Experiments

At the beginning of each experiment, a constant baseline for *f* and *D* was measured with the respective buffer for at least 10 minutes (*i.e.* signal drift ≤ 1 Hz/h for the *f* shift and 1 x 10^6 DU/h for the *D* shift). Afterwards, the tested solutions were allowed to flow through the sensors surfaces. All tested polymeric solutions were freshly prepared immediately prior to use at a concentration of 1 mg/mL in the desired buffer solution. For each experiment, a purified 4 mg/mL GO solution in ultrapure water was used to prepare a 25 μg/mL GO solution in the desired buffer. GO dispersions were homogenized by applying ultrasonic treatment for 5 min before use.

The performed QCM-D experiments are listed in Tables 5 and 6. All experiments were performed at a flow rate of 100 μL/min. Each experiment was performed on both SiO_2- and Ti-coated quartz crystal sensors (*e.g,*. SDS-S and SDS-T were performed on SiO_2 and Ti sensors, respectively). Step 1, Step 2, *etc*. represent the order of the aqueous formulations that were injected in the system. After each new added solution there was a rinsing step with buffer to remove unattached molecules.

Table 5. QCM-D measurements for surfactant and interfactant interaction with SiO_2 and TiO_2 solid surfaces followed by GO adsorption.
Measurements were labeled according to the fist injected aqueous formulation. Used buffers are also presented.

Measurement Label	Buffer	Step 1	Step 2	Step 3
SDS-S SDS-T	Sodium Acetate pH 4.7	SDS	GO	SDS
CTAB-S CTAB-T	Sodium Acetate pH 4.7	CTAB	GO	CTAB
LAC-S LAC-T	Sodium Acetate pH 4.7	LAC	GO	LAC
LYS-S LYS-T	MES pH 6.1	LYS	GO	LYS
PLL-S PLL-T	MES pH 6.1	PLL	GO	PLL

Table 6. QCM-D measurements for LbL adsorption of interfactant molecules and GO on SiO_2 and TiO_2 solid surfaces varying pH conditions.
Measurements were labeled according to the injected aqueous formulations and used buffers.

Measurement Label	Buffer	Step 1	Step 2	Step 3	Step 4	Step 5
LAC-GO-3.6S LAC-GO-3.6T	Sodium Acetate pH 3.6	LAC	GO	LAC	GO	LAC
LAC-GO-4.7S LAC-GO-4.7T	Sodium Acetate pH 4.7	LAC	GO	LAC	GO	LAC
LYS-GO-6.1S LYS-GO-6.1T	MES pH 6.1	LYS	GO	LYS	GO	LYS
LYS-GO-11S LYS-GO-11T	MES pH 11.0	LYS	GO	LYS	GO	LYS
PLL-GO-6.1S PLL-GO-6.1T	MES pH 6.1	PLL	GO	PLL	GO	PLL
PLL-GO-9S PLL-GO-9T	MES pH 9.0	PLL	GO	PLL	GO	PLL

3.2.5 Preparation of samples surfaces for XPS and SEM analysis, antimicrobial and biocompatibility tests

Samples for XPS analysis

A first set of samples for XPS analysis was prepared for studying the chemical composition and layer thickness of analogue surfaces to those studied by QCM-D in Table 6 for the PLL tests. Plasma coated SiO_2 and TiO_2 surfaces were used as substrates. 100 μL of each tested solution was pipetted and dropped on the sample surface. After approximately 1h in contact with the PLL solutions or GO dispersions, the coated substrates were gently rinsed with buffer and the next tested solution was dropped on the substrate. After addition of the last tested solution, the coated substrates were gently rinsed with ultrapure water by applying

a new 100 µL water drop every minute for 4 minutes. Finally, the samples were dried by gently blowing compressed nitrogen gas over the surface and stored under environmental conditions. The PLL solutions were freshly prepared immediately prior to use with a concentration of 1 mg/mL in the desired buffer solution. For each experiment, a purified 4 mg/mL GO dispersion in ultrapure water was used to prepare a 25 µg/mL GO dispersion in the desired buffer. GO dispersions were homogenized by applying ultrasonic treatment for 5 min before use.

Following the QCM-D experiments for PLL described in Table 6, a new sample was prepared for each new added solution up to the second GO layer on both SiO_2 and TiO_2 substrates. For example, considering the measurement PLL-GO-9S, four different samples were prepared. For the first of this samples set, a plasma coated SiO_2 surface was coated with PLL in sodium acetate buffer pH 3.6; a second plasma coated SiO_2 surface was coated with PLL followed by GO; a third one with PLL, followed by GO and PLL; and a forth one covered with PLL followed by GO, PLL and finally GO. Thus, the different prepared samples are listed in Table 7.

Table 7. Samples for XPS analysis.
Samples are labeled according to the used substrate, buffer solution and coating type. Samples were prepared in triplicate.

Sample Label	Buffer	Step 1	Step 2	Step 3	Step 4
S/PLL-6.1 T/PLL-6.1	MES pH 6.1	PLL	-	-	-
S/ PLL-9 T/PLL-9	MES pH 9.0	PLL	-	-	-
S/PLL/GO-6.1 T/PLL/GO-6.1	MES pH 6.1	PLL	GO	-	-
S/PLL/GO-9 T/PLL/GO-9	MES pH 9.0	PLL	GO	-	-
S/PLL/GO/PLL-6.1 T/PLL/GO/PLL-6.1	MES pH 6.1	PLL	GO	PLL	-
S/PLL/GO/PLL-9 T/PLL/GO/PLL-9	MES pH 9.0	PLL	GO	PLL	-
S/PLL/GO/LPLL/GO-6.1 T/PLL/GO/PLL/GO-6.1	MES pH 6.1	PLL	GO	PLL	GO

Samples for SEM analysis

Regarding samples for SEM analysis, 25 µg/mL of commercial GO (original version) and purified GO (purified version) dispersions were prepared in ultrapure water. The original and purified GO versions were analyzed over Si wafers. Additionally, a Si wafer was coated with PLL, followed by GO, PLL and finally GO and the resulting samples was labeled as Si/PLL/GO/PLL/GO. A 0.1 mg/mL PLL solution in MES buffer (30 mM, pH 9.0) was freshly prepared before use. A purified 4 mg/mL GO dispersion in ultrapure water was used to prepare a 25 µg/mL GO dispersion in MES buffer (30 mM, pH 9.0). GO dispersions were homogenized by applying ultrasonic treatment for 5 min before use.

Samples for antimicrobial and biocompatibility tests

Commercial Ti surfaces (6Al4V ELI) were coated for antimicrobial and biocompatible tests. Samples were prepared in the same conditions as the first set of samples for XPS analysis but with a pipetted volume of 500 μL for each tested solution. Prepared samples are listed in Table 8.

Table 8. Prepared samples for SEM analysis.
Samples are labeled according to the used substrate and coating type. Samples were prepared in triplicate.

Sample Label	Buffer	Step 1	Step 2	Step 3	Step 4
Ti/LYS Ti/LYS	MES pH 11.0	LYS	-	-	-
Ti/LYS/GO/LYS/GO Ti/LYS/GO/LYS/GO	MES pH 11.0	LYS	GO	LYS	GO
Ti/PLL Ti/PLL	MES pH 9.0	PLL	-	-	-
Ti/PLL/GO/LPLL/GO Ti/PLL/GO/PLL/GO	MES pH 9.0	PLL	GO	PLL	GO

3.2.6 XPS Measurements

X-ray photoelectron spectroscopy (XPS) is a surface analytical technique for the analysis of material surfaces and permits qualitative and quantitative determination of surface composition. X-rays are used to probe the substrate and electrons from the core levels emitted from a region close to the substrate surface are detected and analyzed using an electron analyzer (Förch *et al.*, 2009). It is based upon a single photon-in/electron-out process where the energy (E) of the photon is given by the Einstein relation:

$$E = hv$$

(Equation 4)

where h is the Plank constant (6.62×10^{-34} J s) and v is the frequency (Hz) of the radiation (Förch *et al.*, 2009). While a photon is absorbed by an atomic core in a molecule or solid, leading to ionization of the atoms, a core electron is emitted from the tested surface. The photon energy exceeding the electron binding energy (E_B) results in a kinetic energy (E_k) of the free electron, with the energy balance as follows (Förch *et al.*, 2009):

$$hv = E_B + E_k$$

(Equation 5)

Fig. 7 shows a schematic representation of core electron emission process during XPS. There is a characteristic binding energy associated with electrons in each core atomic orbital for every atom of any chemical element. Consequently, each element will give rise to a characteristic set of peaks in the photoelectron spectrum. The intensity of the peaks is related to the concentration of the element within the sample region (Förch *et al.*, 2009).

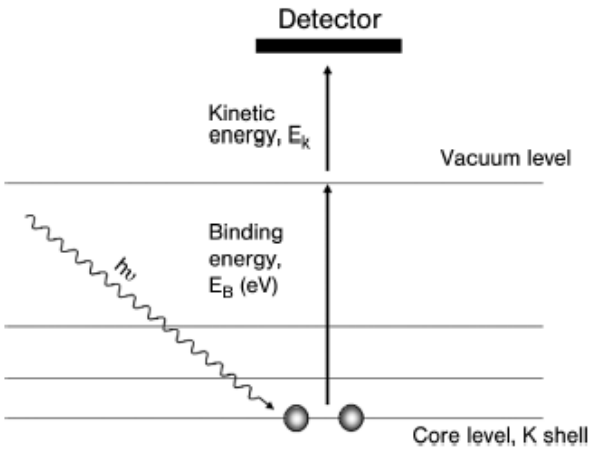

Figure 7. Schematic diagram of the XPS process. (Förch *et al.*, 2009).

XPS measurements were gently performed by Dr. Michael Noeske. XPS spectra were taken using a Kratos AXIS ULTRA system with an information depth of around 0.01 µm and applying excitation of photoelectrons by monochromatic Al K_α radiation within an area of approximately 0.2 mm^2. Further detailed conditions of the measurements were specified by Ureña *et al.*, 2017. The referencing of the binding energy scale for the electrically isolating substrate samples was performed with reference to the C 1s component of ubiquitous (aliphatic) carbon species to 285.0 eV. Atomic concentrations for the detected elements are given in atomic percent (at.%), which are calculated from the relative measured photoelectron intensities. For this calculation, an internal algorithm is applied which is based on assuming an homogeneous sample surface composition. Two positions were investigated for each sample. For calculating the thickness of adsorbates, a compact and homogeneous layer was assumed and the following equation was employed:

$$d = -\ln(y) \times X$$

(Equation 6)

where *d* is the layer thickness, *y* is the Si2p or Ti2p signal intensity ratio between the covered and pristine SiO_2 or TiO_2, respectively, and *X* is the inelastic mean free path of Si2p and Ti2p, assumed to be 3.2 nm in an organic adsorbate layer (Ureña[2] *et al.*, 2016).

3.2.7 SEM Analysis

SEM makes use of a finely focused beam of electrons to produce a high resolution image of a sample. The gun is the scanning electron microscope component that generates the electrons, which after traveling through a column are processed by magnetic lenses and focused at the specimen surface. This beam of high energy electrons is systematically scanned across the surface of the specimen and the generated signals are collected by an electron detector. After converted to photons via a scintillator, the signal is amplified and converted to an electrical signal which will generate an electronic image. A pump system guarantees a high

vacuum mode of operation, minimizing scattering and attenuation of the electron beam before reaching the specimen, avoiding resolution reduction (MyScope, 2017).

SEM examination of the samples was gently performed by Dr. Karsten Thiel. Images were collected in a field emission scanning microscope, type FEI Helios 600 (Dual Bream). The images of the samples were generated at acceleration voltages between 0.5 and 1.0 kV.

3.2.8 Antimicrobial Test

Evaluation of the antimicrobial activity of the coated Ti surfaces was gently performed by Amelie Greif according to the requirements of ISO 22196. Changes were made regarding the sample size ($2\ cm \times 2\ cm$) and observation of bacterial growth for 24 hours at 37 °C was performed under shaking conditions with a multimode microplate reader (Mithras LB 940, Berthold Technologies). Fig. 8 shows a simplified description of the experimental procedure. Samples were prepared in triplicate.

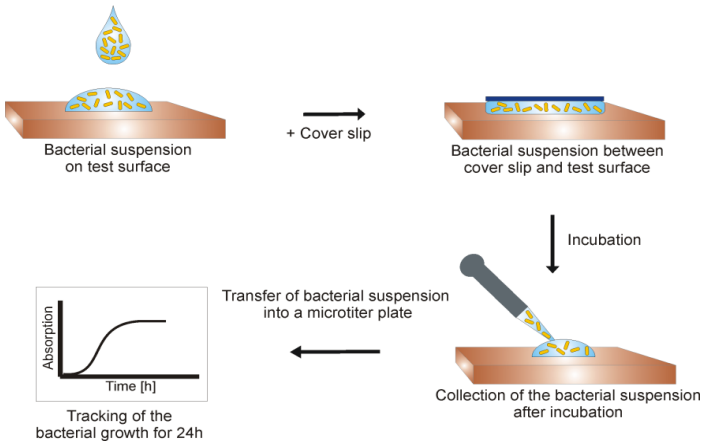

Figure 8. Schematic of the performed experimental procedure for the antimicrobial test. (Gätjen, 2017)

3.2.9 Biocompatibility test

Assessment of biological compatibility of the coated Ti surfaces was gently performed by Amelie Greif according to the requirements of EN ISO 10993-5:2009, in order to evaluate *in vitro* cytotoxicity of the coated surfaces. The test was performed with mouse connective tissue fibroblasts, cell line L929 (DSMZ ACC 2). Samples were prepared in triplicate. Absorbance was measured at 450 nm and the results are presented in % of control ± standard deviation. Fig. 9 shows a simplified description of the experimental procedure.

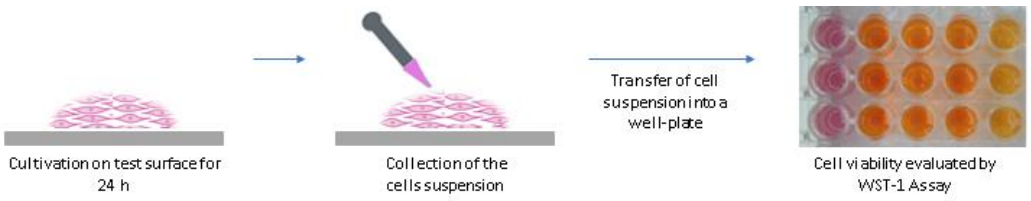

Figure 9. Schematic representation of the performed biocompatibility test.

CHAPTER 4

Results and Discussion

The possibility of interfactant-mediated LbL assembly of GO was investigated by QCM-D and XPS on different substrates. Furthermore, the antimicrobial and biocompatible properties of particular formed layers on Ti substrates were assessed. It is important to mention that XPS analysis was performed to evaluate the surface chemistry of some self-assembled layers as a comparison method against the QCM-D results. Although an effort had been made to use relatively similar SiO_2 and TiO_2 substrates to be coated and analyzed using both techniques, important differences on its nature must be considered. While SiO_2-coated and Ti-coated QCM-D crystals are obtained by physical vapor deposition (PVD) on quartz substrates pre-coated with chromium and gold (BiolinScientific[4]), the substrates used for XPS analysis were obtained by SiO_2 and TiO_2 based thin film coating on Si wafer surfaces using low pressure PECVD. However, considering the passivating surface oxide on titanium (Effah *et al.*, 1995), it was assumed that the Ti test surfaces tend to exhibit a TiO_2-like behavior. In order to compare the different test surfaces, apparent contact angles were measured.

4.1 Purification of GO

In this work, it was used a commercially available dispersion of GO sheets, 4 mg/mL in water. From the elemental analysis performed by Graphenea to 2 g of 0.4 mg/mL GO in water, it was possible to identify a content of 0 – 1% nitrogen and 2 − 4% sulfur, which are elements that are not expected to be found in a pure GO dispersion in water. Furthermore, the XPS spectra also provided by the company revealed an unknown carbon bond (binding energy of ≈ 284.0 eV) in the C1s peak, which also indicates the presence of impurities within the formulation (Graphenea, 2017).

Therefore, GO dispersions were further purified before usage. SEM images were collected before and after purification of the GO dispersion and are presented in Fig. 10. Images on the left side show GO as received, while images on the right side show GO after further purification. By the images on the top, there seems to be a slight decrease on the average GO layer size after purification, which was expected after the repeating centrifugation and ultrasound treatments. Additionally, GO single and multiple sheets could be observed with more detail when analyzing the imagens on the bottom, with the lighter areas representing GO monolayers. Thus, these images also provide confirmation of the GO monolayer content of the used commercial formulation. In order to increase the dispersibility of GO in water, GO dispersions were always treated with ultrasonic bath for 5 min before usage.

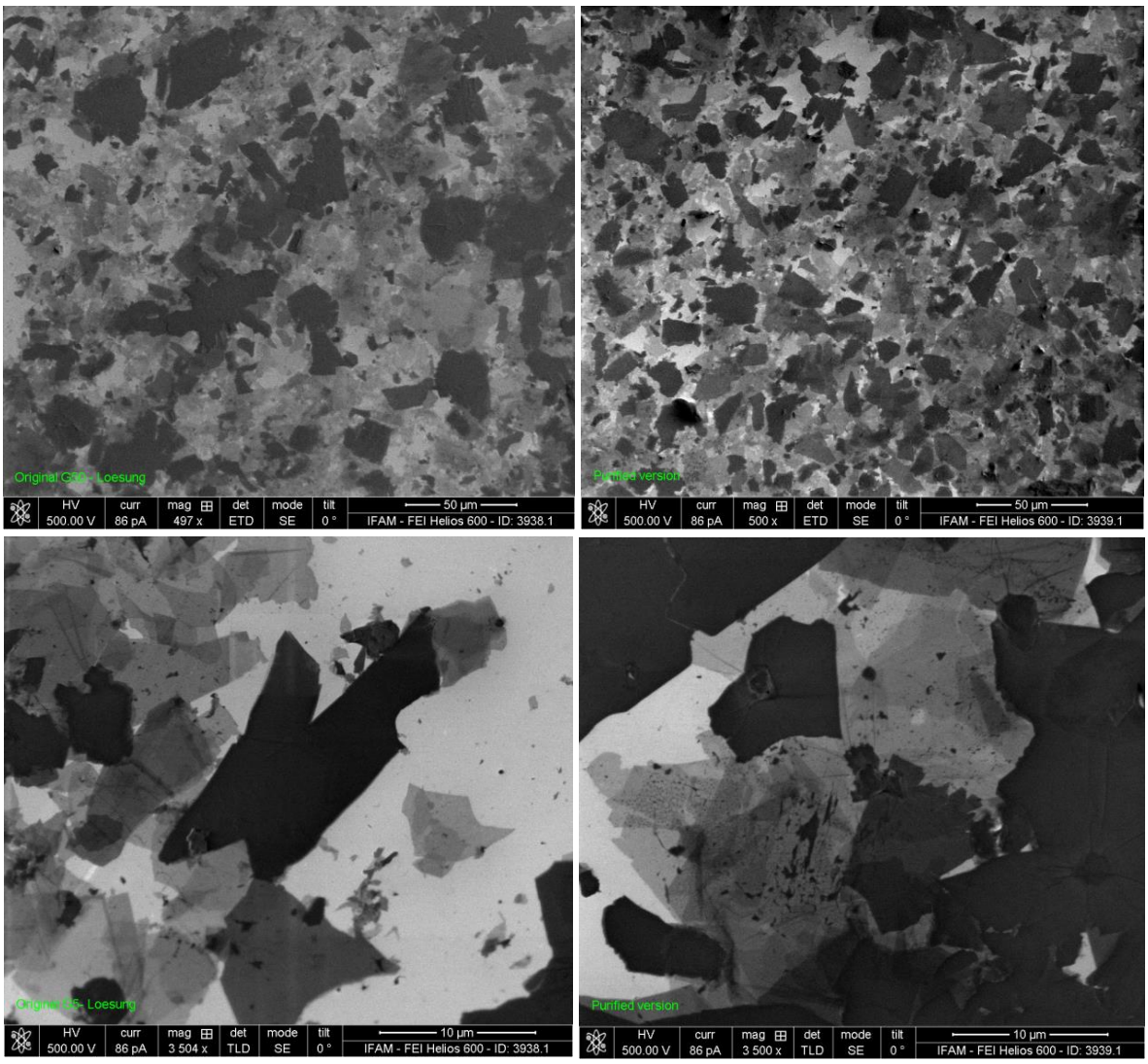

Figure 10. SEM images of the commercial GO before and after purification.
Images on the left and on the right sides correspond to GO before and after purification, respectively. Scale bars correspond to 50 µm (on the top) and 10 µm (on the bottom).

4.2 Contact angle measurement of the different test surfaces

Images of the test surfaces after application of the water droplets and the measured apparent contact angles are presented in Fig. 11. All the test surfaces exhibited a hydrophilic behavior upon contact with water, with measured contact angles below 90° (Förch *et al.*, 2009).

The measured contact angle values for SiO_2 quartz crystal and plasma-coated SiO_2 surfaces were 33.8 ± 1.3° and 33.4 ± 0.4°, respectively. Thus, the wettability of the SiO_2 test surfaces used for QCM-D and XPS experiments was found to be very similar. The measured contact angles of the Ti quartz crystal and plasma-coated TiO_2 surfaces revealed a slightly higher difference in the nature of the test surfaces, with values of 57.0 ± 1.3° and 60.0 ± 1.2°, respectively. A contact angle of 70.6 ± 0.8° was obtained for the Ti 6Al4V ELI surfaces which were coated for the antimicrobial and biocompatibility tests.

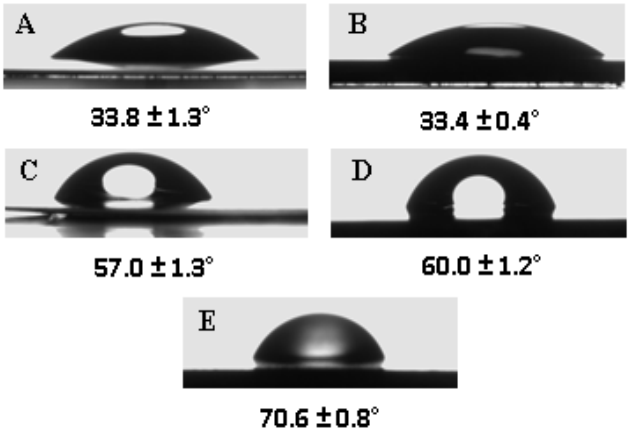

Figure 11. Photographs of the static water contact angles measured on each test surface.
A) SiO_2 quartz crystal surface; B) Plasma-coated SiO_2; C) TiO_2 quartz crystal surface; D) Plasma-coated TiO_2 surface; and E) Ti 6Al4V ELI surface.

4.3 Selection of potential molecules upon directing GO layer formation on SiO_2 and TiO_2 substrates studied by QCM-D

In this section, using QCM-D, the interaction of two different surfactants, sodium dodecyl sulfate (SDS) and hexadecyltrimethylammonium bromide (CTAB), with SiO_2 and TiO_2 surfaces followed by GO adsorption was discussed. Furthermore, LAC, LYS and PLL were discussed as potential interfactants for directing GO layer formation on the studied oxide surfaces. Polymeric interfactants, specifically proteins and peptides, are characterized by strongly attach to a wide range of substrate surfaces (Ureña *et al.*, 2017). Afterwards, if they are able to interact with GO providing a smooth layer formation, the LbL assembly of these biomolecules and GO could be extended to a broad spectrum of solid surfaces.

In the present work, two different oxide surfaces were studied, namely SiO_2 and TiO_2. Its IEP values are usually quoted at a pH < 3 and a pH ranging from 4.7 to 6.2, respectively (Parks, 1965). Depending on the working pH, the net charge of the test surfaces will vary and this is expected to directly influence its interaction with the different adsorbed materials.

4.3.1 Surfactants followed by GO adsorption on SiO_2 and TiO_2 solid surfaces

Different molecules were tested upon directing GO layer formation on the SiO_2 and Ti QCM-D crystal. Firstly, a set of experiments was carried out aiming to distinguish between a typical surfactant- and interfactant-like behavior. In the case of a surfactant, the molecule was expected to loosely attach to the solid substrate and easily swim up on the growing film, while the interfactant was expected to remain at the interface between the substrate and the growing film (Schmidt and Bauer, 2001).

SDS and CTAB were used as anionic and cationic surfactants, respectively. The critical micelle concentration (CMC) of SDS and CTAB is of about 10.0 mM and 1.0 mM, respectively (Sigma-Aldrich[1], 2017; Sigma-Aldrich[2], 2017). 0.1 mg/mL of SDS and CTAB corresponds to a molar concentration of 0.35

mM and 0.27 mM, respectively (appendix C-2). Both surfactants were used below the CMC, which means that its adsorption on oppositely charged surfaces is expected to be essentially due to electrostatic interaction between individual isolated charged monomeric species and the positively charged solid surface (Zhang and Somasundaran, 2006).

Analyzing Fig. 10, when SDS was flushed over the SiO_2 surface (SDS-S, stage II) no significant Δf was observed, indicating no material deposition. Also after GO injection there was no Δf as it would be predicted by the presented results in Fig. 12. Subsequently, no interaction between the anionic surfactant SDS and the negatively charged SiO_2 surface was assumed due to electrostatic repulsion between the molecule and the surface (Holmberg, 2003). In the case of the Ti sensor surface, a Δf of approximately – 4 Hz was observed after SDS injection and rinsing (SDS-T, stage III), indicating that SDS deposited on the surface and was stable upon rinsing. Anion adsorption can be nonspecific or specific. Nonspecific adsorption involves only electrostatic attraction while specific adsorption occurs by ligand exchange. Interestingly, sulfate (SO_4^{2-}) is one of the few anions that can be adsorbed specifically (Maynard, 1998). Based on this assumption, the anionic SO_4^{2-} ions of SDS head group might have dislocated a hydroxyl (OH^-) group of the TiO_2 surface and bonded directly to a metal center on the surface. This would be consistent with a ligand exchange mechanism of adsorption for SDS on TiO_2.

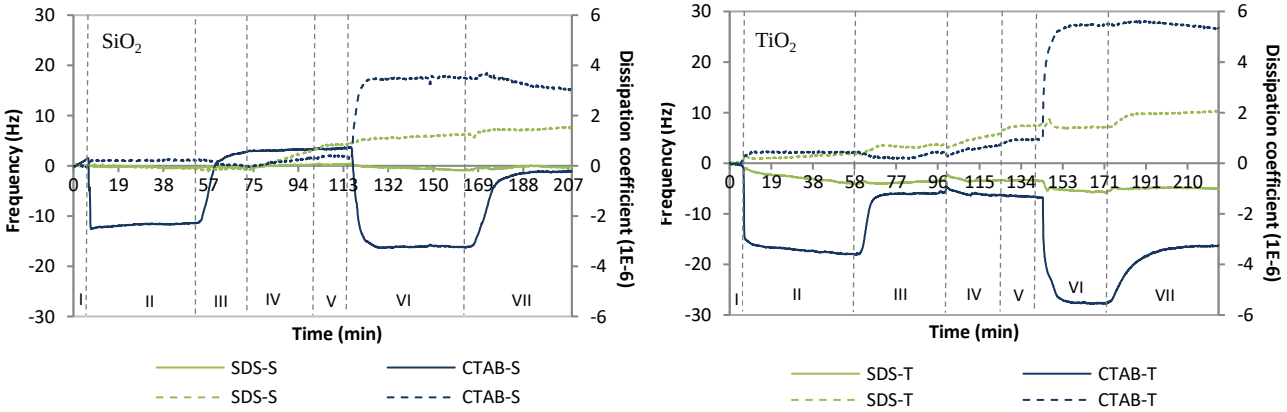

Figure 12. QCM-D results for surfactants interaction with SiO_2 and TiO_2 solid surfaces followed by GO injection.
Results of *f* (solid line) and *D* (dashed line) shifts at the 5th overtone (Δf_5 and ΔD_5) as a function of time on SiO_2 (left side chart) and Ti (right side chart) QCM-D sensors. A baseline with 0.2 M sodium acetate buffer was stablished on stage I. 0.1 mg/mL SDS and CTAB solutions were flushed over the crystals surface (stage II) followed by 25 µg/mL GO dispersion (stage IV) and SDS and CTAB solutions (stage VI). A rinsing step with 0.2 M sodium acetate buffer pH 4.7 was introduced after every new injected solution (stages III, V, VII).

After GO injection and rinsing (SDS-T, stage V), although no significant Δf could be observed, there was a ΔD of about 1.0 DU from stage III to stage V. The viscoelastic adsorbed mass was modeled using the software Q-Sense Dfind (Biolin Scientific, Sweden). An absorbed mass of 431 ng/cm^2 and 1020 ng/cm^2 was obtained for the stages III and V, following the Smart Fit viscoelastic model (appendix A–Figure 1). These results clearly indicated an interaction between the adsorbed SDS on the Ti sensor surface and GO, which might be related to hydrophobic interactions between GO graphitic patches and the SDS hydrocarbon tails. However, since no significant Δf was observed, this mass uptake may be related to trapped

water within the formed layers due to conformation changes of the pre-adsorbed SDS molecules, as suggested by the detected Δ*D*.

Analyzing CTAB interaction with the SiO_2 surface, a Δ*f* of about – 12 Hz was verified on stage II (Fig. 12), with no significant Δ*D*, indicating formation of a rigidly attached material (Vashist and Vashist, 2011). This interaction is attributed to electrostatic attraction between the negatively charged SiO_2 and the positively charged CTAB head groups (Liset *et al.*, 2013). In the second CTAB injection (stage VI), a Δ*f* of about – 16 Hz was verified accompanied by a sudden increase in *D* of about 3.5 DU, indicating formation of a dissipative attached material (Vashist and Vashist, 2011). These formed CTAB layers on the SiO_2 surface were instable during rinsing with buffer (stage III and VII). In both cases after CTAB deposition, highly positive *f* shifts to values close to zero were observed, indicating mass desorption from the crystal surface. The viscoelastic modeled adsorbed mass was 28 ng/cm^2 after rinsing for the first CTAB deposited layer (stage III) and 1555 ng/cm^2 for the second CTAB formed layer (stage VIII) (appendix A–Figure 1).

After GO injection and rinsing (CTAB-S), an increase in the absorbed mass of approximately 99 ng/cm^2 from stage IV to stage V was obtained (appendix A–Figure 1). This was assumed as result of the interaction between the negatively charged GO and the remaining CTAB molecules at the SiO_2 surface. In fact, Meng and co-workers reported complexation of GO and CTAB, indicating that this interaction is dominated by electrostatics and also hydrophobic interaction may arise between GO graphitic patches and CTAB hydrocarbon tails (Meng *et al.*, 2015).

In the case of CTAB interaction with the Ti sensor surface, also a Δ*f* of about – 18 Hz and – 21 Hz for the first and second injections of CTAB (stages II and VI) was verified, respectively. The adsorbed CTAB was heavily desorbed from the Ti sensor surface after the rinsing steps (stages III and VII). The modeled adsorbed mass was 108 ng/cm^2 after rinsing for the first CTAB formed layer (stage III) and 203 ng/cm^2 for the second CTAB adsorbed layer (stage VII) (appendix A–Figure 1). Thus, the adsorbed mass in the first CTAB injection increased in a factor of 2 to the second CTAB injection. This might have been influenced by complexation with the injected GO and by water uptake within the formed layers, as suggested by the high Δ*D* verified on stage VI.

Considering the IEP of TiO_2 at a pH that may vary between 4.7 and 6.1, at the buffer pH of 4.7, the surface may vary from neutral to slightly positively charged. Thus, a negligible amount of CTAB would be expected to adsorb onto the solid surface, since it would electrostatically repeal the cationic surfactant. However, the above presented results show that a significant amount of CTAB adsorbs to TiO_2 even when the surface has probably no negative net charge. This was attributed to dispersion forces between the hydrocarbon chain of the CTAB molecule and the surface which promoted adsorption. Overall, the substrate surface was either neutral or slightly positively charged, but the CTAB could still bind to the few negatively charged sites. Consequently, these bonded molecules act as an anchor for further adsorption by hydrophobic interactions of the hydrocarbon chains (Walsh *et al.*, 2014).

Finally, it is interesting to observe that higher Δ*f* are not always related to higher mass absorption or desorption as it would be expected from the point of view of a rigid material adsorption onto a solid surface. It should be also noticed that Sauerbrey equation is only strictly valid for rigid, nonporous, homogeneous layers (Vashist and Vashist, 2011). For example, when SDS and CTAB were allowed to flow over the Ti sensor surfaces followed by rinsing (stage IV), a more negative *f* value was reached after equilibrium for CTAB-T rather than for SDS-T. However, in the second case, the adsorbed mass was 431 ng/cm^2, which is a higher value in comparison with the CTAB adsorbed mass of 108 ng/cm^2 in the same stage. This reflects the valuable contribution of *D* for the mass estimation of viscoelastic adsorbed films (Cai *et al.*, 2015).

4.3.2 Interfactants followed by GO adsorption on SiO_2 and TiO_2 solid surfaces

As analyzed before, the use of surfactants for directing LbL assembly of GO onto solid oxide surfaces did not reveal promising results mainly due to surfactant instability on the solid surface upon rinsing. Additionally, the nature of the GO-surfactant interactions mainly dominated by electrostatic might limit the process to the use of cationic surfactants. On the other hand, polymeric interfactants may provide promising prospects on this field since they are characterized by strongly attach to a wide range of substrate surfaces. Thus, two different proteins and one polypeptide, laccase (LAC), lysozyme (LYS) and poly-L-lysine (PLL), respectively, were tested as interfactants upon directing GO layer formation on SiO_2 and Ti sensor surfaces (Fig. 13).

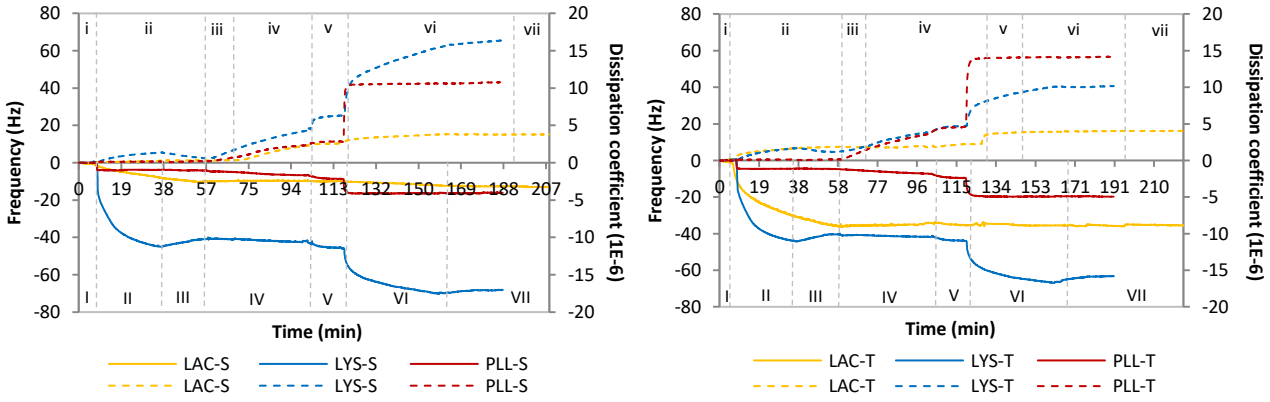

Figure 13. QCM-D results for interfactants interaction with SiO_2 and TiO_2 solid surfaces followed by GO injection. Results of *f* (solid line) and *D* (dashed line) shifts at the 5th overtone (Δf_5 and ΔD_5) as a function of time on SiO_2 (left side chart) and Ti (right side chart) QCM-D sensors. A baseline with 0.2 M sodium acetate buffer pH 4.7 (in the case of LAC) and with 20 mM MES buffer pH 6.1 (in the case of LYS and PLL) were stablished on stages i and II, respectively. Vertical dashed lines on the top and stages i to viii refer to LAC experiments on both surfaces. Vertical dashed lines on the bottom and stages I to VIII refer to LYS and PLL experiments. 0.1 mg/mL LAC (stage ii), LYS and PLL (stage II) solutions were flushed over the surfaces followed by 25 μg/mL GO (stage iv and IV) dispersion and 0.1 mg/mL LAC (stage vi), LYS and PLL (stage VI) solutions in the respective buffers. Rinsing steps were introduced after every new injected solution (stages iii, v and viii and stages III, V and VIII).

Regarding the first injection of interfactants, all *f* shifts reveal a rigid material adsorption on both substrates with Δ*D* up to 1.5 DU (stage ii for experiments LAC-S and LAC-T and stage II for experiments

LYS-S, LYS-T, PLL-S and PLL-T). Additionally, all the deposited interfactant layers were irreversibly attached to the surfaces, with no significant Δ*f* upon rinsing for LAC and PLL, and with a slight Δ*f* of 3 Hz in the case of LYS on both substrates (stages iii and III). Several studies have suggested that after protein adsorption onto a solid surface, its removal from the aqueous phase or washing does not cause the protein to desorb from the substrate (Westwood *et al.*, 2012; Ureña[1] *et al.*, 2016). After GO injection on stages iv and IV, very low Δ*f* could be observed. However, except for LAC-T where no significant Δ*D* took place, a Δ*D* of about 2.1 DU for LAC-S, 5.2 DU for LYS-S, 3.4 for LYS-T, 2.7 DU for PLL-S and 4.4 DU for PLL-T could be observed after rinsing (steps v and V). These positive *D* shifts might indicate GO interaction with the interfactant layer materials which in turn resulted into dissipative attached materials. In fact, the modeled adsorbed mass increased from stages iii and III to v and V (appendix A–Figure 2), which could indicate GO adsorption on the growing film. However, considering the high Δ*D* compared with the low Δ*f* in the same stages, the apparent increase in the desorbed mass on the growing films may also be related to water uptake upon conformational change of the interfactant molecules. These different possibilities are discussed in the following sub-chapter.

For the second interfactant injection steps (vi and VI), for both PLL and LYS experiments on SiO_2 and Ti sensor surfaces, the negative Δ*f* together with positive Δ*D* indicated a new interfactant layer deposition. By the higher Δ*D* observed in stages vi and VI, it is interesting to observe that the second interfactant injection after interaction with GO resulted in deposition of a dissipative attached material, in contrast with the first rigidly attached interfactant formed layer. This might indicate the differences between interfactant-substrate and interfactant-GO interfaces regarding structural or conformational properties of the adsorbed molecules. Upon adsorption, proteins and peptides undergo conformational changes due to its interactions with the solid surface (Westwood *et al.*, 2012). Thus, it is natural to assume that the different nature of the substrates (*i.e.*, SiO_2, TiO_2 and GO) affected the structure of the adsorbed interfactant films.

Overall, the obtained results dictated a progressive increase of the adsorbed mass on the substrates after each new added material, revealing a good prospective for LbL assembly between the tested interfactants and GO. The absorbed mass (ng/cm^2) and thickness (nm) were modeled following the Smart Fit viscoelastic model and the results can be consulted in appendix A–Figure 2 and B–Table 2, respectively.

4.4 LbL assembly of interfactants and GO on SiO_2 and TiO_2 surfaces studied by QCM-D

On of most important factors to be considered when studying LbL assembly of biomolecules and GO is the working pH (Zhang *et al.*, 2016). Usually, the pH would be selected so that protein or polypeptide and GO have net opposite charges based on the IEP of these molecules. At the same time, apart from electrostatic attraction, other interactions of hydrophobic nature as well as π-π staking interactions have been reported to play an important role on proteins or polypeptides and GO interactions (Georgakilas *et al*., 2012).

Based on the above-mentioned facts, LbL assembly of the studied interfactants and GO was tested on SiO_2 and TiO_2 surfaces under two different pH conditions: pH at the IEP of the interfactant and pH below

the IEP of the interfactant. In the first case, the interfactant exhibits a neutral net charge, and in the second case a positive net charge. Colloidal graphene oxide can be considered as a material with a negative surface charge due to its high amount of acidic groups (Haubner *et al.*, 2010).

4.4.1 LbL assembly of LAC and GO

The used LAC in the present study was laccase C from *Trametes versicolor* with an IEP at the pH of about 4.7 (Ureña[2] *et al.*, 2016). Most fungal LACs are monomeric globular enzymatic proteins with a molecular weight of ranging from 60 to 100 kDa (Madhavi *et al.*, 2009). By QCM-D, 0.1 mg/mL LAC solutions in 0.2 M sodium acetate buffer, pH 4.7 and pH 3.6, where tested upon LbL assembly with 25 µg/mL GO in the same buffer conditions on SiO_2 and TiO_2 surfaces. The results are presented in Fig. 14 for the working pH of 4.7 and 3.6 on the top and bottom charts, respectively.

Regarding the first injection of LAC (stage II), for both pH 4.7 and 3.6, a considerable lower Δf could be observed on SiO_2 ($\Delta f = -17$ Hz) sensor surface comparing with Ti ($\Delta f = -35$ Hz) sensor surface. For both LAC-GO-4.7S and LAC-GO-3.6S, steady state was not reached after more than 70 min of contact time with the suspension, indicating the low affinity of the biopolymer for adsorption on SiO_2. This difference is also very clear when observing the results of the adsorbed mass for the first LAC layer formation on both substrates (Fig. 15). On the other hand, also a slower decrease in the f was observed in the early stages of the biofilm growth on the SiO_2 substrate compared to the TiO_2 substrate. Electrostatic interaction is not enough to explain the preferred binding of LAC to TiO_2 over SiO_2 since the surface charge of TiO_2 (IEP $\approx$ 4.7 to 6.2) and SiO_2 (IEP < 3) would suggest that LAC stronger adheres to SiO_2. Thus, it is likely that other factors, such as material-specific structure or localized surface charges, also contributed to the binding selectivity of the protein coating (Khoo *et al.*, 2009).

The modeled adsorbed mass after rinsing for the first LAC injection (stage III) of 361 ng/cm^2 on SiO_2 (LAC-GO-4.7S) was very similar to that reported by Ureña[2] and co-workers, which was also result of LAC adsorption on SiO_2 under pH conditions close to the IEP of the protein (Ureña[2] *et al.*, 2016). Values between 250 and 500 ng/cm^2 may be expected as a rule of thumb in a typical protein monolayer (Ureña[1] *et al.*, 2016). At the pH of 4.7, under conditions close to the IEP of the protein, there is a very low electrostatic repulsion between protein molecules and neighboring protein. Comparing LAC adsorbed mass after its first injection on LAC-GO-4.7S and LAC-GO-4.7T with the adsorbed mass on LAC-GO-3.6S and LAC-GO-3.6T (Fig. 15), it was clear that close to its IEP, LAC absorbed more and stronger to the surfaces, since the desorbed mass after rinsing was also higher at pH 4.7.

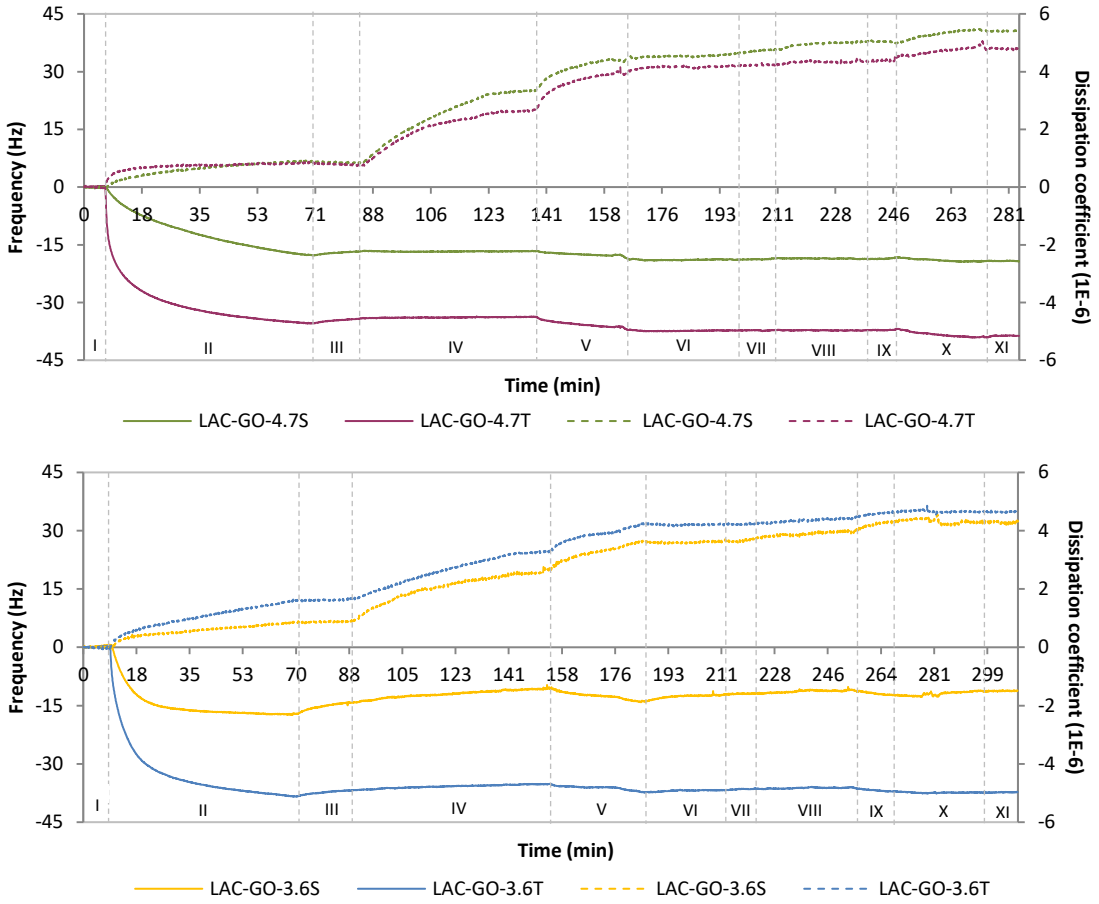

Figure 14. QCM-D results for the LbL assembly of LAC and GO on SiO_2 and TiO_2 solid surfaces under different pH conditions.
Results of QCM-D measurements for *f* (solid line) and *D* (dashed line) shifts at the 5th overtone (Δf_5 and ΔD_5) as a function of time on SiO_2 and Ti QCM-D sensors. A baseline with 0.2 M sodium acetate buffer, pH 4.7 (top chart) and pH 3.6 (bottom chart), were stablished on stages I. 0.1 mg/mL LAC in sodium acetate buffer was flushed over the surfaces (stages II), followed by 25 µg/mL GO (stages IV), 0.1 mg/mL LAC (stages VI), 25 µg/mL GO (stages VIII) and 0.1 mg/mL LAC (stages X) in the respective buffers. There was a rinsing step with buffer after every new injected solution (stages III, V, VIII and IX).

Analyzing Fig. 14, stage IV, although the Δf in every measurement seemed to be not significant, the observed ΔD dictated an increase in the estimated adsorbed mass, as it was shown for all experiments upon GO first injection (Fig. 15). However, due to the observed evolution of the *f* shifts during stages IV and V, attribution of this mass increase to GO adsorption might be not considered. Observing the adsorbed mass up to the rinsing step after the first GO injection, it was clear that the highest mass uptake occurred in the experiment LAC-GO-4.7T. The difference in the adsorbed mass between the second and the first rinsing steps was of about 557 ng/cm^2, which corresponds to the final mass uptake after GO first injection. The estimated viscoelastic thickness of this new formed layer was approximately 1.3 nm (appendix B–Table 3). However, QCM-D response is very sensitive to the viscoelastic properties of any mass coupled to the quartz crystal, which may include the adsorbed molecules of interest, water and salt coupled to the molecule layers (Westwood *et al.*, 2012). Thus, estimated mass either by Sauerbrey or Smart Fit viscoelastic models will always be a hydrated mass. Consequently, GO injection might have promoted a considerable change in the structural properties of the pre-adsorbed LAC films, which was accompanied by water uptake within the

interfactant layer, promoting a considerable positive *D* shift. These conformational changes were attributed to interactions between LAC and GO, which were more pronounced on TiO_2 at a pH of 4.7. Nevertheless, strong LAC adsorption to the solid surfaces might have limited its structural conformation to an extent that did not allow GO layer formation.

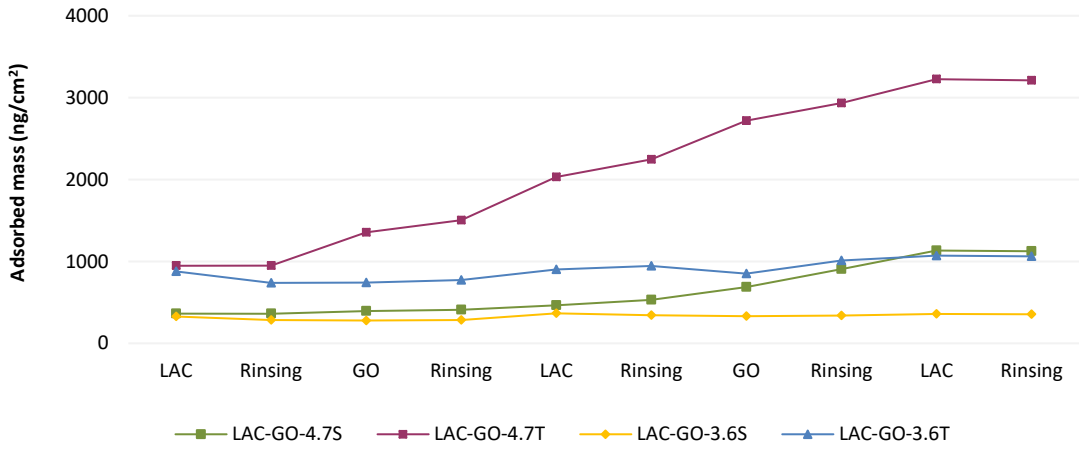

Figure 15. Viscoelastic modelling of the adsorbed mass for LbL assembly of LAC and GO.
Results of the cumulative modeled adsorbed mass (ng/cm^2) for LAC-GO-4.7S, LAC-GO-4.7T, LAC-GO-3.6S and LAC-GO-3.6T experiments. QCM-D data was modeled following the Smart Fit viscoelastic model for each new added layer and rinsing steps.

As discussed before, LAC preferred to adsorb on TiO_2 under pH conditions close to its IEP. Inclusively, LAC adsorption on LAC-GO-4.7T and LAC-GO-3.6T with estimated adsorbed masses of approximately 947 and 877 ng/cm^2, respectively, was considerably higher than the expected values for a typical protein monolayer. Thus, these results suggested bilayer formation, with proteins in the second layer possibly more loosely bonded, which might have directed a stronger interaction with GO under pH 4.7. Since under these pH conditions LAC had a net charge close to zero, electrostatic interaction was probably playing no predominant role on its interaction with GO. Several works have shown that LAC can interact with different molecules by hydrophobic interactions based on its characteristic hydrophobic pocket composed of hydrophobic amino acids (Lalaoui *et al.*, 2016; Bertrand *et al.*, 2002). Inclusively, there was no tendency for mass uptake under pH 3.6 upon GO injection, even when the used substrate was favorable for the interfactant bilayer formation, in the case of LAC-GO-3.6T. There was even a slight positive Δf, which may indicate LAC desorption from the surface. Moreover, here is also an increased instability of GO colloidal suspensions under low pH conditions, since the number of protonated carboxyl groups at the edges of the GO sheets increases such that GO becomes less hydrophilic and form aggregates (Shih *et al.*, 2012).

On the second LAC injection (Fig. 14, stages VI), no significant Δf could be observed for the performed experiments. This indicates that no second LAC layer was adsorbed which was also in agreement with the supposition that no GO layer had been deposited before. Finally, the performed experiments seemed to meet no favorable conditions for LbL assembly of LAC and GO on the studied solid surfaces.

4.4.2 LbL assembly of LYS and GO

The used LYS in this work has an IEP at a pH of about 11.0 (Li *et al.*, 2014). LYS is a small monomeric globular enzymatic protein with a molecular weight of approximately 14 kDa (Li *et al.*, 2014). By QCM-D, 0.1 mg/mL LYS solutions in 30 mM MES buffer, pH 11.0 and pH 6.1, where tested upon LbL assembly with 25 µg/mL GO in the same buffer conditions on SiO_2 and TiO_2 surfaces. Results are present in Fig. 16 for the working pH of 4.7 and 3.6 on the top and bottom charts, respectively.

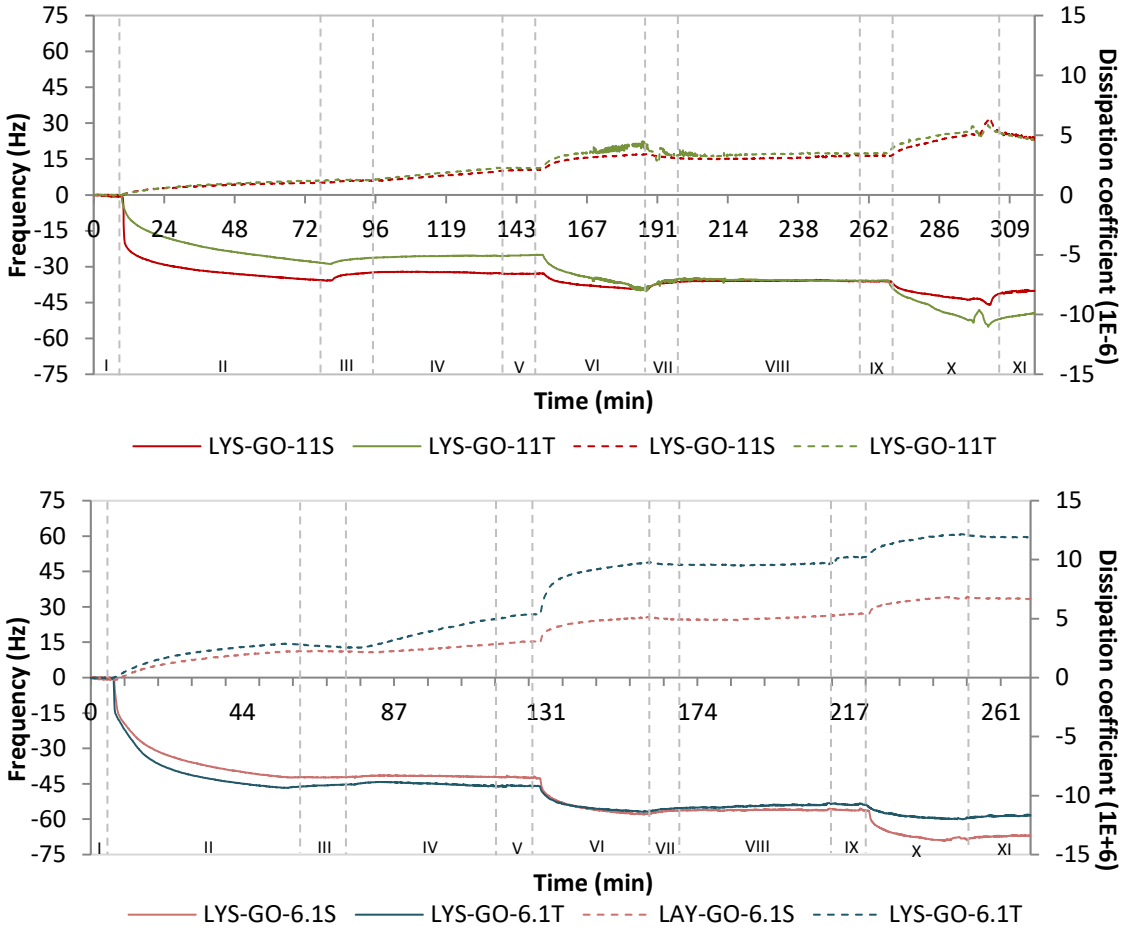

Figure 16. QCM-D results for the LbL assembly of LYS and GO on SiO_2 and TiO_2 solid surfaces under different pH conditions.
Results of QCM-D measurements for *f* (solid line) and *D* (dashed line) shifts at the 5th overtone (Δf_5 and ΔD_5) as a function of time on SiO_2 and Ti QCM-D sensors. A baseline with 30 mM MES buffer, pH 11 (top chart) and pH 6.1 (bottom chart), were stablished on stages I. 0.1 mg/mL LYS in MES buffer was flushed over the surfaces (stages II), followed by 25 µg/mL GO (stages IV), 0.1 mg/mL LYS (stages VI), 25 µg/mL GO (stages VIII) and 0.1 mg/mL LYS (stages X) in the respective buffer. There was a rinsing step with buffer after every new injected solution (stages III, V, VIII and IX).

Regarding the first LYS injection (Fig. 16, stages II) on both tested pH and substrates, the observed negative *f* shifts dictated a strong adsorption of the protein to the solid surfaces. The low Δf upon rinsing (Fig. 16, stages III) indicated that the material was irreversibly attached to the surface. Analyzing the adsorbed mass after the first LYS injection and rinsing (Fig. 17), the protein tended to show a slightly stronger interaction with the surfaces at pH of 6.1 rather than at pH 11.0. This difference could be explained

by the negative net charge that both surfaces tend to exhibit at this working pH, which could have favored a stronger adsorption of the positively charged LYS even when there is a tendency for electrostatic repulsion between the interfactant molecules. However, this only holds true for the first minutes of absorption. Saturation of the protein-substrate interface can take several hours to be reached (Choi *et al.*, 2015). Adsorption rates tend to be higher when protein and substrate bear opposite charges since electrostatic attractions accelerate the migration towards the surface (Rabe *et al.*, 2011). Nevertheless, since electrostatic protein-protein repulsions are minimized at the IEP (allowing a higher packing on the surface), total mass load is generally found to be maximized at the IEP (Choi *et al.*, 2015; Khoo *et al.*, 2009).

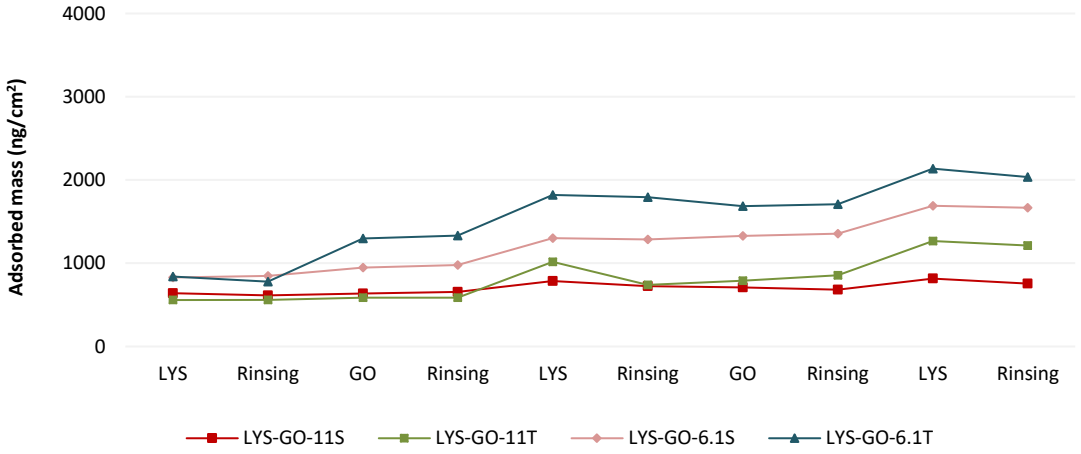

Figure 17. Viscoelastic modelling of the adsorbed mass for LbL assembly of LYS and GO.
Results of the cumulative modeled adsorbed mass (ng/cm^2) for LYS-GO-11S, LYS-GO-11T, LYS-GO-6.1S and LYS-GO-6.1T experiments. QCM-D data was modeled following the Smart Fit viscoelastic model for each new added layer and rinsing steps.

Lu *et al.* have shown that a thin (≈ 1 nm) but dense LYS layer is formed on a hydrophobic surface, with a layer density of 1.28 g/cm^3, whereas a much thicker (≈ 6 nm) but less dense LYS layer is formed on a hydrophilic surface (Lu *et al.*, 1998). Taking into account the hydrophilicity of the used substrates in this study, LYS would be expected to form a 6 nm thick layer on SiO_2 and TiO_2. However, the estimated layer thickness after LYS injection and rinsing was only 2.32 nm and 2.12 nm on SiO_2 and TiO_2, respectively (appendix B–Table 4). In this case, it was concluded that for the experiments LYS-GO-11S and LYS-GO-11T, the complete coverage of the surfaces had not been reached after approximately 80 minutes of exposure.

Considering the first GO injection and rinsing (Fig. 16, stages IV), the Δf was considered not significant over the performed experiments, except for LAC-GO-6.1T where a slightly negative f shit was observed. However, this Δf was accompanied by a significant ΔD in all experiments, which determined an increase in the estimated absorbed mass. For the experiment LYS-GO-6.1T, the estimated mass uptake was of about 555 ng/cm^2. This is a value that must be taking into account, but its attribution to absorption of GO within the growing films is a question that has to be considered with caution. In fact, LYS interaction with GO has been already reported and mainly attributed to electrostatic interactions in solution at a pH below

the IEP of the protein (Li *et al.*, 2014). Inclusively, Smith and co-workers investigated LYS adsorption capacity of GO, graphene and single-walled CNTs, having concluded that GO exhibits the highest adsorption capacity among the three tested materials at the equilibrium (Smith *et al.*, 2014). They have also reported that another cause for a greater affinity of LYS for GO could be their hydrophilic nature which facilitated mutual interaction. However, in the previously mentioned studies, LYS and GO interaction was studied with the protein in solution. In this study, a solid support was introduced on which the interaction of GO with the immobilized protein was limited by the interfactant pre-acquired conformation at the surface. This means that the possibility of LbL assembly of interfactants and GO was not only dependent on the GO-interfactant interactions, but also dependent on the protein-surface interface.

By the obtained results, it seemed to be that for the tested pH and substrates, the interaction between LYS and GO was very limited and the results were not enough to insure GO layer formation. One common factor among the obtained results was the increase in *D* upon GO injection, which is likely to originate from energy dissipation within the protein layer due to capillary-like water between the adsorbed proteins (Höök *et al.*, 1998), as previously verified in the last sub-chapter, in the case of LAC. Thus, GO could have interacted with the already formed interfactant layer in such a way that some of the positive domains of the LYS, which used to face the negatively charged substrates, tended to suffer an internal rearrangement within the monolayer due to electrostatic attraction with the negatively charged GO. This conformational change increased the viscoelastic properties of the coating resulting in capillary water uptake, which explains the increased adsorbed mass after the first GO injection (Fig. 17).

Analyzing the following stages, it was clear that for both GO injections and rinsing steps (Fig. 16, stages V and IX) there was a tendency for LYS adsorption, as indicated by the negative *f* shifts on stages VI and X. Inclusively, it was possible to observe that the adsorption rate in the first minutes was quite high, being followed by a second phase of LYS adsorption at a lower rate, which described a typical kinetic model of protein adsorption to a solid surface (Höök *et al.*, 1998). This phenomenon could be explained by three different possibilities: 1) there was GO adsorption on stages VI and VIII, followed by a new LYS layer formation; 2) there was protein desorption during GO injection, followed by LYS mass uptake when the surfaces where again exposed to the interfactant molecule; 3) or there was no GO adsorption neither LYS desorption during GO injection and there is another factor which is allowing formation of a second LYS layer in these specific conditions (*e.g.*, ionic strength, buffer interference).

4.4.3 LbL assembly of PLL and GO

The used PLL in this work was poly-L-Lysine hydrochloride with a molecular weight between 15 and 30 kDa (Sigma-Aldrich, Germany). PLL is a polymer composed of lysine amino acids with an IEP at a pH ranging from 9.0 to 11 (Choi *et al.*, 2015). It is known to spontaneously adsorb onto various types of materials, although the amount of PLL adsorption to solid surfaces is usually reported to be low (Choi *et al.*, 2015). As a result, a very low surface coverage is often obtained with an average thickness of about 1

nm (Westwood et al., 2012; Jordan *et al.*, 1994). By QCM-D, 0.1 mg/mL LYS solutions in 30 mM MES buffer, pH 11.0 and pH 6.1, were tested upon LbL assembly with 25 µg/mL GO in the same buffer conditions on SiO_2 and TiO_2 surfaces. Results are present in Fig. 18 for the working pH of 9.0 and 6.1 on the top and bottom charts, respectively.

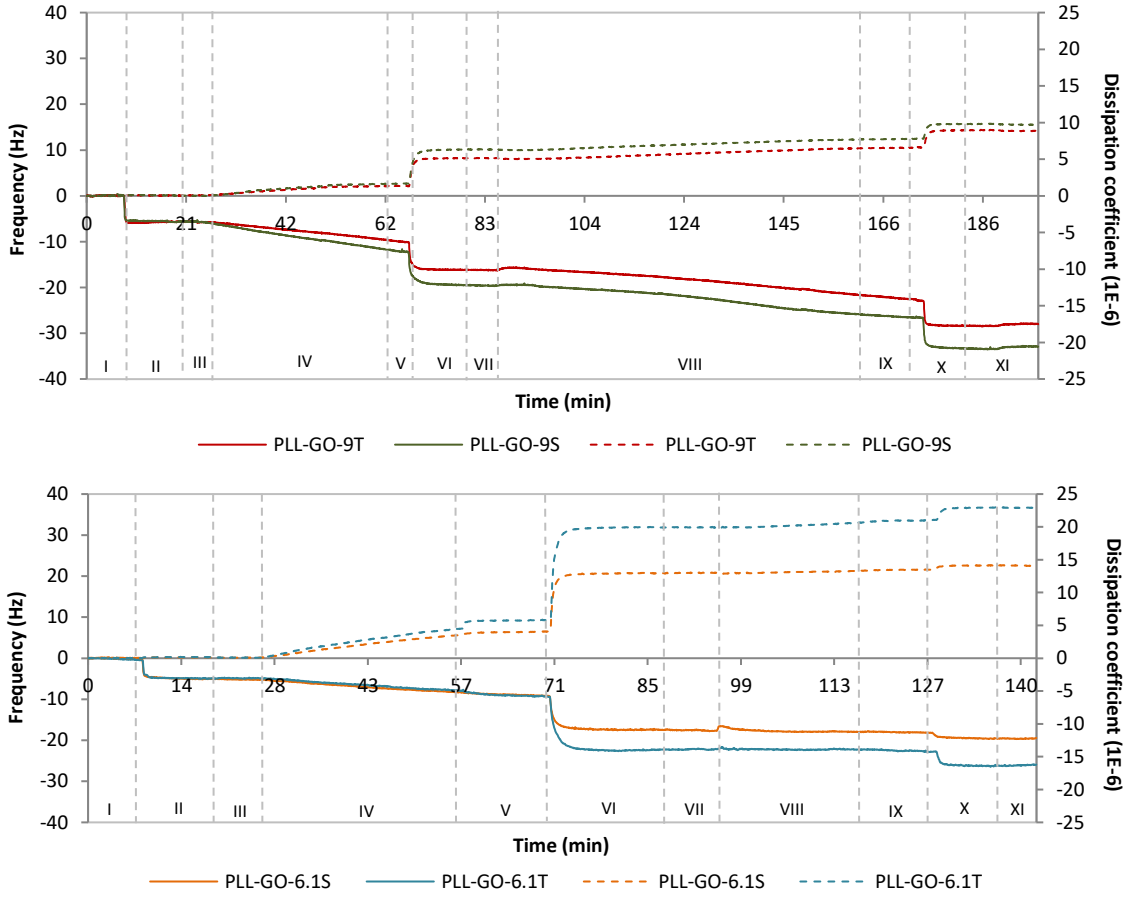

Figure 18. QCM-D results for the LbL assembly of PLL and GO on SiO_2 and TiO_2 solid surfaces under different pH conditions.
Results of QCM-D measurements for *f* (solid line) and *D* (dashed line) shifts at the 5th overtone (Δf_5 and ΔD_5) as a function of time on SiO_2 and Ti QCM-D sensors. A baseline with 30 mM MES buffer, pH 9 (top chart) and pH 6.1 (bottom chart), were stablished on stages I. 0.1 mg/mL PLL in MES buffer was flushed over the surfaces (stages II), followed by 25 µg/mL GO (stages IV), 0.1 mg/mL PLL (stages VI), 25 µg/mL GO (stages VIII) and 0.1 mg/mL PLL (stages X) in the respective buffer. There was a rinsing step with buffer after every new injected solution (stages III, V, VIII and IX).

For the first PLL injection and rising steps (Fig. 18, stages II and III) on both tested pH and substrates, a negative Δf was observed together with no significant ΔD, indicating PLL adsorption on the surfaces as a rigid film. This adsorption was low compared with the already studied interfactants (LAC and LYS) and characterized by a rapid single adsorption step, with a plateau region being reached after approximately 2 minutes for all performed experiments. Additionally, the adsorbed material was very stable upon rinsing, with no Δf verified on stage III. Choi and co-workers obtained very similar results for PLL adsorption on SiO_2 QCM-D sensors, with a Δf after rinsing of about – 5 Hz and – 6 Hz under pH 6.0 and 9.0, respectively (Choi *et al.*, 2015). Analyzing the modeled adsorbed mass in Fig. 19, there was a higher tendency for PLL adsorption on SiO_2 and TiO_2 under pH 9.0 rather than at pH 6.1. This seems to be

consistent with an isoelectric mechanism of adsorption, since close to the IEP there is a minimization of the electrostatic repulsion between the polyelectrolyte chains. Porus and co-workers investigated PLL adsorption onto SiO_2 solid supports, having demonstrated that from pH 4 to 11, PLL uptake on SiO_2 generally increases with the solution pH (Porus *et al.*, 2012). As discussed before, the nature of the substrate affects the adsorption process. The higher affinity of PLL for adsorption on TiO_2 rather than on SiO_2 was revealed by the modeled adsorbed mass after the first PLL injection and rinsing, where a slightly higher adsorption was estimated on TiO_2 under the same pH conditions.

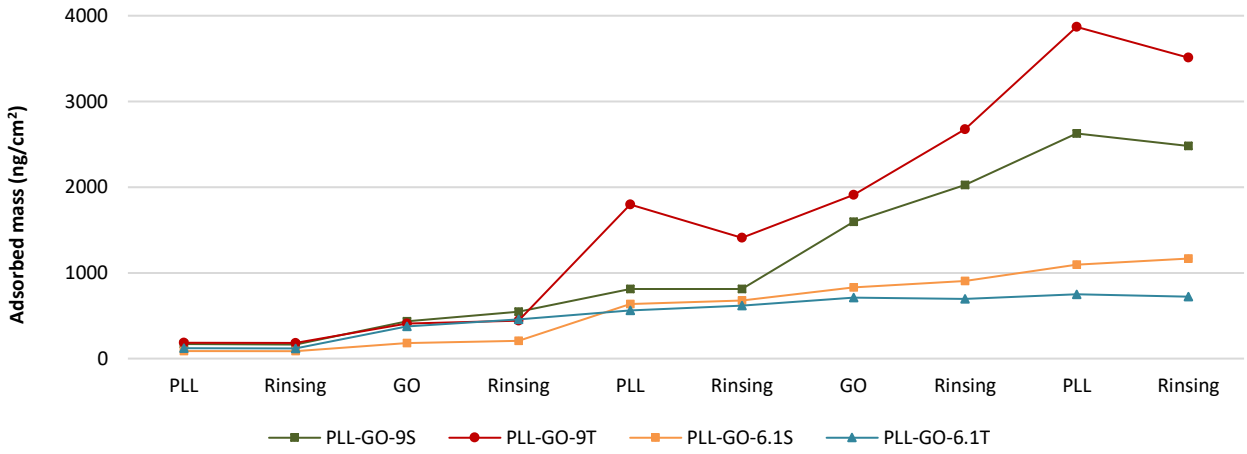

Figure 19. Viscoelastic modelling of the adsorbed mass for LbL assembly of PLL and GO.
Results of the cumulative viscoelastic modeled adsorbed mass (ng/cm^2) for PLL-GO-9S, PLL-GO-9T, PLL-GO-6.1S and PLL-GO-6.1T experiments. QCM-D data was modeled following the Smart Fit viscoelastic model for each new added layer and rinsing steps.

Injection of GO (Fig. 18, stage IV) was accompanied by a linear negative Δf, indicating GO adsorption on the PLL pre-coated substrates. Moreover, a significant ΔD revealed the viscoelastic properties of the adsorbed films. By the modeled adsorbed mass (Fig. 19), GO adsorption for PLL-GO-6.1S was very low, with a mass uptake of only 122 ng/cm^2 after GO injection and rinsing, which corresponded to an estimated thickness of 0.3 nm (appendix B–Table 5). This result was under the expected value for the dry thickness of a GO monolayer, which is expected to be around 1 nm (Lin, 2012). This phenomenon was attributed to the low coverage of interfactant obtained in the previous steps (stages II and III) which consequently might have induced a weaker interaction with GO molecules. In the other cases, the estimated adsorbed masses were significantly higher and the estimated thicknesses were closer to an expected GO monolayer. An increase in the thickness of 0.96 nm, 0.65 nm and 0.85 nm was estimated after GO injection for PLL-GO-9S, PLL-GO-9T and PLL-GO-6.1T, respectively (appendix B–Table 5).

When considering an electrostatic mechanism of adsorption, GO molecules would be expected to adsorb more on the PLL pre-coated substrates under pH 6.1. However, by the obtained results for the estimated mass upon GO injection, this tendency was not very clear. Regarding the GO chemical structure, the edge phenolic hydroxyl and carboxyl groups make more contributions to its negative surface charge compared with the basal-plane hydroxyl and epoxy groups (Haubner *et al.*, 2010). For this reason, GO

molecules interaction with a PLL formed layer by hydrophobic interactions would be favored when the polypeptide chains exhibit a net charge closer to neutrality, under pH 9.0. In a review article involving graphene and GO interactions with proteins and peptides, Zhang and co-workers stated that different works have indicated hydrophobic interactions between proteins and graphene (or chemically rGO) as stronger than electrostatic interaction between tested proteins and GO (Zhang *et al.*, 2013). Thus, a parallelism to the obtained results in this work could be stablished in such a way that close to its IEP, PLL hydrocarbon chains may strongly interact by hydrophobic interaction with the GO basal-plane (which may preserve some hydrophobic domains and tends to be less negatively charged comparing to the GO edges). The above-mentioned statements may justify differences in the GO adsorbed masses between PLL-GO-9S and PLL-GO-6.1S. However, concerning the experiments PLL-GO-9T and PLL-GO-6.1T the mass uptake after first GO injection and rinsing was relatively close. This fact may represent one more indication of the influence of the substrate nature on the adsorption process.

Additionally, it was interesting to observe the difference in the ΔD after the first GO injection. Between stages III and V, D increased up to 6 DU for the working pH of 6.1 and only up to 2 DU when the pH was 9.0, for both tested substrates. This tendency was also very clear on stages VI and VII, when upon PLL second injection, ΔD was much more pronounced under pH 6.1. Thus, GO adsorption on PLL-coated substrates under pH 6.1 resulted in highly dissipative attached materials, while under pH 9 the growing films tended to be more rigid. Furthermore, PLL second injection (stages VI) was accompanied by a slightly higher Δf comparing with its first injection (stages II). Generally, there was a significantly higher mass uptake upon second PLL injection (Fig. 19), which was more evident under pH 9.0. As already mentioned, the higher stability of the polypeptide under pH conditions closer to its IEP, may have guaranteed a higher tendency for GO layer formation in the following steps (stages VIII). On the other hand, it is also important to consider the higher ΔD after PLL second injection, which may also have contributed to a higher adsorbed mass due to trapped water within the viscoelastic formed films. This hypothesis was further explored in the following sub-chapter.

Overall, increase of the estimated adsorbed mass after each new added material suggested promising prospects for LbL assembly of PLL and GO under specific pH conditions. Although the presented results indicated that PLL-GO-9S and PLL-GO-9T comprised the most favorable conditions among the tested ones, it is worth mentioning that the ideal pH conditions for LbL assembly of a specific interfactant and GO might not be constant within the growing film. In this specific study, using the same buffer solution over time was a constraint that guaranteed more feasible results for the QCM-D experiments, since a stable base line with buffer was stablished in the beginning of each experiment with both f and D showing no significant variation around 0 Hz and 0 DU, respectively. Finally, PLL adsorption under pH 9.0 seems to be the condition allowing a higher coverage of the solid surface. However, GO adsorption under pH 6.1 onto a PLL pre-coated substrate under pH 9.0 would be a very important experiment for clarifying the influence of the pH conditions concerning LbL assembly of PLL and GO. Thus, it would be possible to assess how a closed and

stable PLL monolayer, formed in the most favorable conditions on a solid surface, would interact with GO when the molecules exhibit opposite net charges.

Regarding all tested interfactants, under the studied pH conditions and substrates, LAC and LYS showed no clear potential for LbL assembly with GO by the QCM-D investigations. Influences of the substrate, working pH, as well as possible forces governing protein-substrate, protein-protein and protein-GO interactions were discussed. The characterization of these interfaces represents a very challenging task taking into account the high complexity of these macromolecules. However, the obtained results may reveal that the conformational changes these proteins undergo upon adsorption have limited its interactions with GO. On the other hand, PLL was the most promising among the tested interfactants and could successfully direct GO layer formation on SiO_2 and TiO_2 surfaces. In order to investigate this finding in more detail, LbL assembly of PLL and GO was studied by XPS and the results were presented in the following section.

4.5 LbL assembly of PLL and GO on SiO_2 and TiO_2 surfaces studied by XPS

As information depth of XPS is approximately 10 nm (Ureña[1] *et al.*, 2016), spectroscopic investigations of thin adsorbates on SiO_2 and TiO_2 substrates facilitate the assessment of the compositions of the adsorbates, which were thinner than 10 nm according to the QCM-D estimated thickness for the PLL experiments (appendix B-Table 5), even when these last ones are in the wet state. Thus, a new sample surface was coated for each adsorption step through a traditional LbL assembly process according to the QCM-D experiments using PLL as interfactant (Fig. 18). The chemical composition of the thus treated SiO_2 and TiO_2 sample surfaces was investigated by XPS. The results are presented in Tables 9 and 10 for SiO_2 and TiO_2 coated surfaces, respectively. As a benchmark, the elemental composition of the pristine substrates was also investigated.

In general, for the SiO_2 samples, the XPS investigations detected silicon, oxygen, carbon, nitrogen species as well as trace amounts of sodium species below 0.4 at.%. For the TiO_2 samples, the XPS investigations detected titanium, oxygen, carbon and nitrogen species as well as trace amounts of silicon, argon and silver species below 1 at.% (contaminants introduced during the plasma coating process). In all cases there was a tendency for a decrease of the Si and Ti atomic concentrations and increase in the C and N at.% within the growing films, which was an indication that the materials were being deposited step-by-step.

Based on the GO chemical composition (Fig. 1), adsorption of the molecule is expected to contribute with C and O species for the elemental surface composition evaluated by XPS. On the other hand, based on the PLL chemical composition (Pubchem[1], 2017), adsorption of the molecule is expected to contribute with C, O and N species for the elemental surface composition. Consequently, increase in the N surface concentration within the growing films was exclusively attributed to PLL adsorption, using N as a maker element for the poly amino acid. For all the tested surfaces and pH values, it was observed an increase in the [N] upon PLL exposure, which is attributed to a first PLL layer formation on the pristine substrates, on

the coated samples named S/PLL-9, S/PLL-6.1, T/PLL-9 and T/PLL-6. The formation of a second PLL layer was concluded for the samples S/PLL/GO/PLL-9, S/PLL/GO/PLL-6.1, T/PLL/GO/PLL-9, T/PLL/GO/PLL-6.1. Additionally, there was a decrease in the [N] upon exposure to GO (*i.e.*, S/PLL/GO-9, S/PLL/GO/PLL/GO-9, *etc.*). At the same time, [C] increased continuously upon new layer formation in for all the tested substrates and pH, which was expected taking into account that the adsorb molecules are mainly based in C species.

Table 9. Results of the XPS investigations for the coated SiO_2 surfaces.
Elemental surface compositions are given in at.%, for pristine plasma-coated SiO_2 surfaces and for the same substrates after contact for 1 h with 0.1 mg/mL PLL and 25 µg/mL GO buffered aqueous formulations (30 mM MES buffer, pH 9.0, on the left and 30 mM MES buffer, pH 6.1, on the right) in the order indicated by the sample label. For each sample two positions were investigated. Average values are given and standard deviations are presented in appendix B-Table 6.

Sample	[Si] (at.%)	[O] (at.%)	[C] (at.%)	[N] (at.%)
Pristine SiO_2	28.9	60.5	10.3	0.2
S/PLL-9	27.8	57.5	13.0	1.3
S/PLL/GO-9	23.6	52.0	22.7	1.3
S/PLL/GO/PLL-9	24.3	51.8	21.6	2.0
S/PLL/GO/PLL/GO-9	20.8	48.0	28.7	2.2

Sample	[Si] (at.%)	[O] (at.%)	[C] (at.%)	[N] (at.%)
Pristine SiO_2	28.9	60.5	10.3	0.2
S/PLL-6.1	27.7	56.9	14.4	1.0
S/PLL/GO-6.1	26.9	56.6	16.0	0.6
S/PLL/GO/PLL-6.1	25.7	54.3	18.6	1.4
S/PLL/GO/PLL/GO-6.1	22.2	51.5	25.2	1.2

Table 10. Results of the XPS investigations for the coated TiO_2 surfaces.
Elemental surface compositions are given in at.%, for pristine plasma-coated TiO_2 surfaces and for the same substrates after contact for 1 h with 0.1 mg/mL PLL and 25 µg/mL GO buffered aqueous formulations (30 mM MES buffer, pH 9.0, on the left and 30 mM MES buffer, pH 6.1, on the right) in the order indicated by the sample label. For each sample two positions were investigated. Average values are given and standard deviations are presented in appendix B-Table 7.

Sample	[Ti] (at.%)	[O] (at.%)	[C] (at.%)	[N] (at.%)
Pristine TiO_2	23.2	53.3	0.2	0.8
T/PLL-9	19.8	47.7	26.9	3.6
T/PLL/GO-9	16.3	43.7	34.9	3.2
T/PLL/GO/PLL-9	15.1	41.0	37.8	4.4
T/PLL/GO/PLL/GO-9	13.0	38.9	42.9	3.8

Sample	[Ti] (at.%)	[O] (at.%)	[C] (at.%)	[N] (at.%)
Pristine TiO_2	23.2	53.3	0.2	0.8
T/PLL-6.1	21.6	49.5	24.3	2.8
T/PLL/GO-6.1	17.1	45.0	33.9	2.4
T/PLL/GO/PLL-6.1	15.5	41.6	37.8	3.5
T/PLL/GO/PLL/GO-6.1	12.7	39.5	43.7	2.8

PLL is a polymer of the amino acid L-lysine, whose chemical structure is presented in Fig. 20. Since each amino acid contains two O and two N atoms, the expected variation in the [O] and [N] detected by XPS upon exposure of the surfaces to peptide is expected to be the same for these two elements. However, since the amount of O containing groups in the GO molecules is unknown and the tested surfaces are also rich in O species, the interpretation of its [O] evolution was considered very complex and, thus, it was not shown.

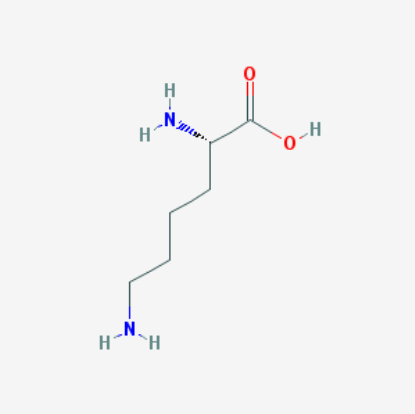

Figure 20. Lysine 2D structure.
The oxygen-containing groups are colored in red and the nitrogen-containing groups in blue. (PubChem[2], 2017).

Fig. 21 shows the evolution in the [N] within the growing films for all tested surfaces and pH values. Additionally, the attenuation of the Si2p and Ti2p substrate signals may be deduced by the $[Si]/[Si]_{pristine}$ and $[Ti]/[Ti]_{pristine}$ concentration ratios, respectively. As mentioned before, attenuation of the Si2p and Ti2p substrate signals revealed material deposition in the growing films. There was attenuation of the substrate signals upon PLL and GO exposure, which means that both molecules were adsorbing at the surfaces. In detail, the attenuation was higher for TiO_2 substrates on both working pH, dictating a higher amount of deposited material. Attenuation of the Ti2p substrate signals of more than 40% was observed in the end of the last adsorption step, while a value below 30% was detected in the case of the Si2p substrate signals.

By the [N] evolution upon performing the successive steps of the LbL assembly process, there was always an increase of the N surface concentration upon PLL exposure. This was followed by a decrease in the [N] which is a consequence of the N1s signal attenuation due to GO deposition, except for S/PLL/GO/PLL/GO where an increase in the [N] was detected. This phenomenon was interpreted to be a consequence of using independent samples for LbL assembly of the tested molecules. Moreover, N surface concentration can be used as a qualitative and quantitative indicator for the polypeptide adsorption. The highest increase in the [N] was always verified for the first PLL layer formed on the pristine substrate surfaces (*i.e.*, S/PLL-9, S/PLL-6.1, T/PLL-9 and T/PLL-6.1) rather than for the second PLL layer formed on the GO pre-covered samples (*i.e.*, S/PLL/GO/PLL-9, S/PLL/GO/PLL-6.1, T/PLL/GO/PLL-9 and T/PLL/GO/PLL-6.1). This finding appears not to be in agreement with the QCM-D results that, following the interpretations based on the applied viscoelastic model, rather indicated a higher PLL adsorption in the second case. As discussed in the previous sections, the higher ΔD verified upon PLL second injection determined adoption of a dissipative attached material, whose viscoelastic properties are characterized by a large amount of trapped water within the polymer adsorbed layer. Thus, when considering as well the QCM-D signals for immersed samples and the XPS signals for dry samples, one may suggest that this trapped

water is accounted for the PLL mass estimation, which resulted in a higher adsorbed mass upon second PLL injection.

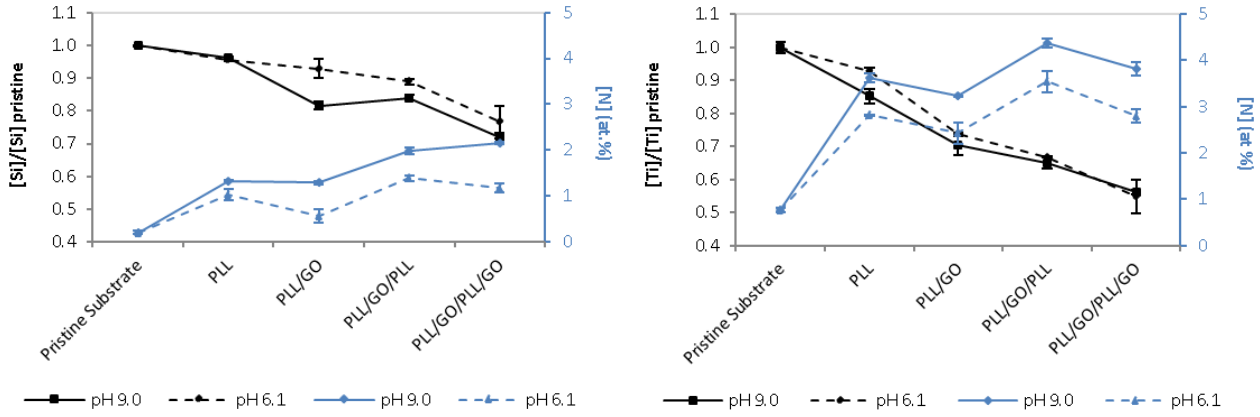

Figure 21. Attenuation of the Si2p and Ti2p signals and evolution of the N surface concentration.
[Si]/[Si] $_{pristine}$ and [N] at.% for each sample according to the XPS results presented in Tables 9 and 10 for the SiO_2 and TiO_2 substrates, respectively.

A deeper analysis of this phenomenon was accomplished by calculating the thickness of the dry films based on the XPS results. Results are presented in Fig. 22, together with the results for the modeled thickness obtained from the equivalent performed QCM-D experiments shown by Fig. 18. By comparison of the obtained results for the different techniques, the highest thickness among the 4-layer substrate/PLL/GO/PLL/GO samples was obtained for the TiO_2 substrate under pH 9.0. It is important to observe that both techniques determined a smaller thickness of the final coating when pH varied from 9.0 to 6.1 on the same substrate. While the final dry thickness obtained from XPS investigations was higher on TiO_2 for both working pH values comparing with the SiO_2 substrate, QCM-D results revealed a final wet thickness that tends to be higher under pH 9.0 independently of the used substrate. By these findings, important considerations about the viscoelastic properties of the adsorbed PLL and GO layers could be made. It was assumed that PLL adsorption onto a pre-coated GO surface under pH 9.0 promoted formation of a much softer wet film comparing with PLL adsorption onto the pristine substrates. This possibility was already stated in the previous section and could be confirmed by comparison with the XPS results of dry layer systems.

Under pH 9.0, up to the first GO layer formation, the estimated thickness using both techniques was relatively similar. For example, 0.31 ± 0.08 nm and 0.46 nm were detected after the first PLL layer formation on TiO_2 (pH 9.0) by XPS and QCM-D (samples PLL, TiO_2 – pH 9), respectively. However, 1.00 ± 0.06 nm and 3.53 nm were detected after the second PLL layer formation by XPS and QCM-D (samples PLL/GO/PLL, TiO_2 – pH 9), respectively. Thus, this difference between the QCM-D and XPS-derived mass was attributed to solvent molecules coupled to the adsorbed polypeptide layer, which in the second case was much higher due to change in the viscoelastic properties of the formed layers.

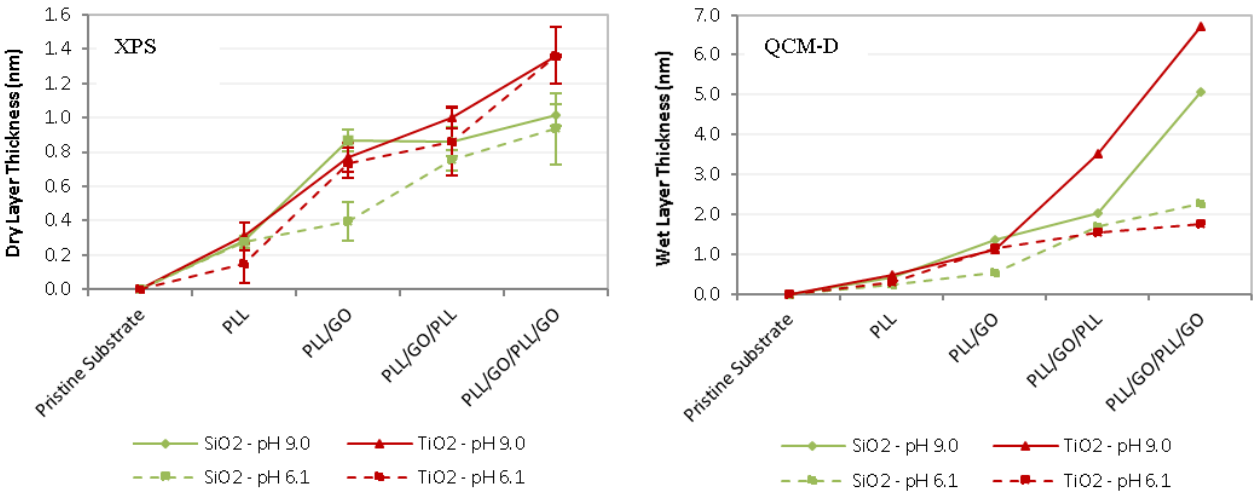

Figure 22. Comparison between the calculated layer thickness by XPS and the viscoelastic modeled thickness by QCM-D. On the left, layer thickness of the dry films calculated based on the XPS results for the samples presented in Tables 9 and 10. On the right, layer thickness of the wet films based on the QCM-D results and estimated according to the Smart Fit viscoelastic model for the measurements shown in Figure 16. The estimated thickness is presented after rinsing for each new added solution.

In the last section, it was proposed that the most favorable conditions for LbL adsorption of PLL and GO could require varying pH within the assembly process. Analyzing the first and second GO layer deposition on TiO_2, the dry thickness calculated from XPS results indicated a higher adsorption under pH 6.0 rather than pH 9.0. On the other hand, PLL adsorption seems to be higher under pH 9.0, as already discussed in the last section. It is also interesting to observe that a higher GO adsorption was verified always on TiO_2 rather than on SiO_2 (even when this is more pronounced under pH 6.1), indicating an influence of the substrate upon GO adsorption, with this influence being mediated by the interfactant adsorbate and its properties.

Concerning the surface functionalization process involving the use of PLL as a polymeric interfactant for directing GO layer formation, the QCM-D experiments together with the XPS investigations suggested the construction of a multilayer system which is simply exemplified in Fig. 23.

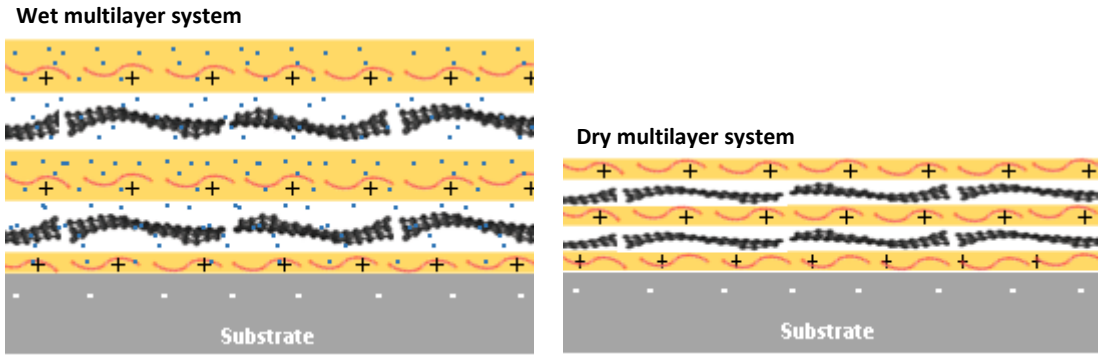

Figure 23. Sketch showing the proposed multilayer system for LbL assembly of PLL and GO on a negatively charged substrate.
On the wet multilayer system, the positively charged PLL layers (yellow layers) and negatively charged GO layers are expected to show higher thickness after the first GO layer formation due to the presence of trapped water within layers, as compared to the dry multilayer system.

4.6 GO adsorbates on PLL-coated SiO_2 surfaces studied by SEM

Samples with minor coverage of GO were prepared and investigated by XPS and SEM. Natively oxidized Si wafer coated by twice dipping in PLL and GO formulations, respectively, generating the sample Si/PLL/GO/PLL/GO. XPS investigations indicated minor coverage (results not shown). In this way, laterally separated GO nanosheets were prepared and investigated by SEM (Fig. 24).

Analyzing Fig. 24, although every GO dispersion had been treated for 5 min with ultrasound before usage, some GO nanosheets were found not to be single flakes. This may be attributed presumably to π-π stacking among the single layers. Bilayer formation is indicated in the images by dashed arrows. Additionally, by the image on the left, GO shows a sheet like morphology with some wrinkles (white arrow). By the image on the right side, the PLL-coated substrate could direct GO single layer formation with mostly smooth basal planes and sharp edges (full black arrow).

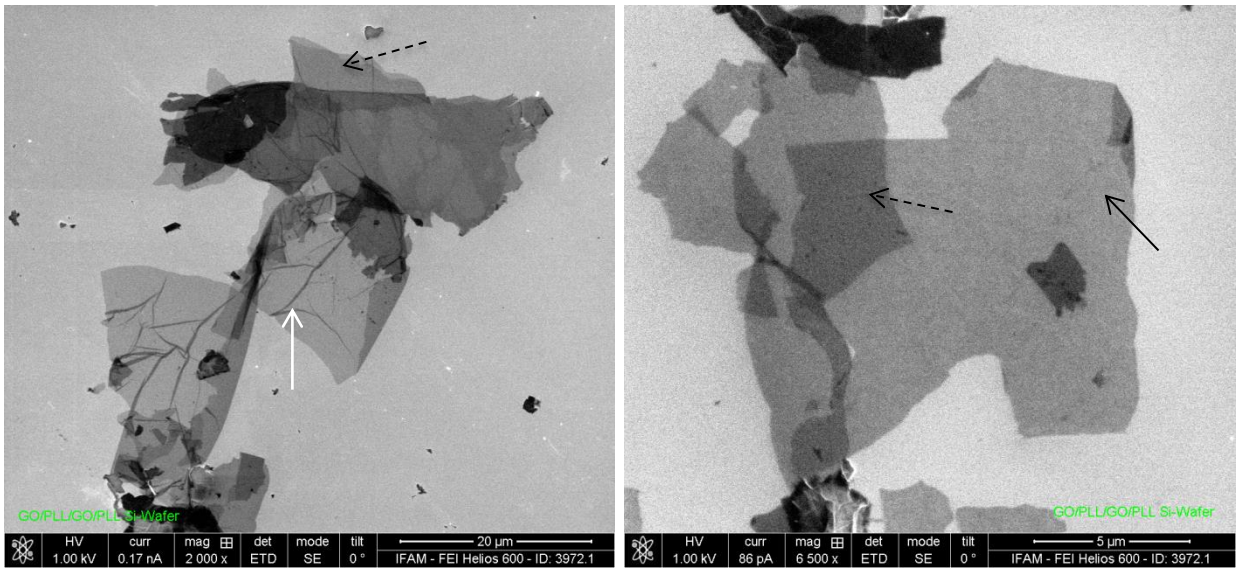

Figure 24. SEM images of PLL/GO/PLL/GO-coated Si wafer.
The scale bars correspond to 20 µm (on the left) and 5 µm (on the right). Full black, dashed black and white arrows indicate GO monolayers, GO bilayers and wrinkles on the GO sheets, respectively.

4.7 Antimicrobial and biocompatible properties of interfactants and GO self-assembled monolayers

The potential antimicrobial activity of commercial Ti surfaces (6Al4V ELI, ARA-T Advance, Germany) coated with LYS, PLL and GO were tested against *E. coli*. The bacterial growth curves were observed over 24 h at 37 °C and are presented in Fig. 25. LYS is an antibacterial enzyme which hydrolyzes the peptidoglycan present in the bacterial cell walls. It is extremely abundant in human tears, being part of the innate immune system (Li *et al.*, 2014). PLL has an antimicrobial activity which is well documented, but its mechanism of action is only vaguely described. Hyldgaard and co-works studied the antimicrobial mechanism of action of PLL against *E. coli* and hypostasized that PLL destabilizes the bacterial membranes

in a carpet-like mechanism by interacting with negatively charged phospholipid head groups (Hyldgaard *et al.*, 2014).

Analyzing Fig. 25, the negative control, consisting of applying Luria-Bertani (LB) on the non-antimicrobial Ti surface, showed no bacterial growth. The Ti/LYS surface resulted in a normal bacterial growth curve exhibiting a clear lag phase up to approximately 2 h, followed by an exponential phase in which *E. coli* was growing and dividing at the maximal rate (from 2 h up to approximately 4 h). Finally, after 4 h, there was a tendency for population stabilization and the rate of cell death started approaching the rate of cell division. However, a clear stationary phase could not be observed after 24 h. Thus, this sample did not retard bacterial growth to any important extent. Although in solution LYS is found to be antimicrobial, adsorption onto the Ti surface possibly changed its conformation to an extent that resulted in the loss of its enzyme activity, and consequent loss of antibacterial activity. Similarly, it has been reported that LYS adsorption onto silica nanoparticles results in loss of its activity owing to the loss of α–helices in its structure compared with that of "free" lysozyme (Vertegel *et al.*, 2004). Regarding the Ti/LYS/GO/LYS/GO sample, there was also no bacterial growth inhibition. By the QCM-D results, there was no clear evidence of GO adsorption on the LYS-coated solid surfaces. Inclusively, the possibility of some LYS desorption upon GO exposure was stated. This possibility was reinforced by the last presented results, since the Ti/LYS/GO/LYS/GO sample showed a higher growth compared to the Ti/LYS sample. Thus, the LYS coating showed to be less favorable for *E. coli* growth compared to the hypothesized almost naked Ti surface represented by the Ti/LYS/GO/LYS/GO sample. For the Ti/PLL sample, there was bacterial growth inhibition for 9 h. This was followed by a short exponential phase with low growth rate and the stationary phase was stablished after approximately 12 h. Additionally, on the stationary phase the observed growth was approximately three times lower comparing with that of the Ti/LYS.

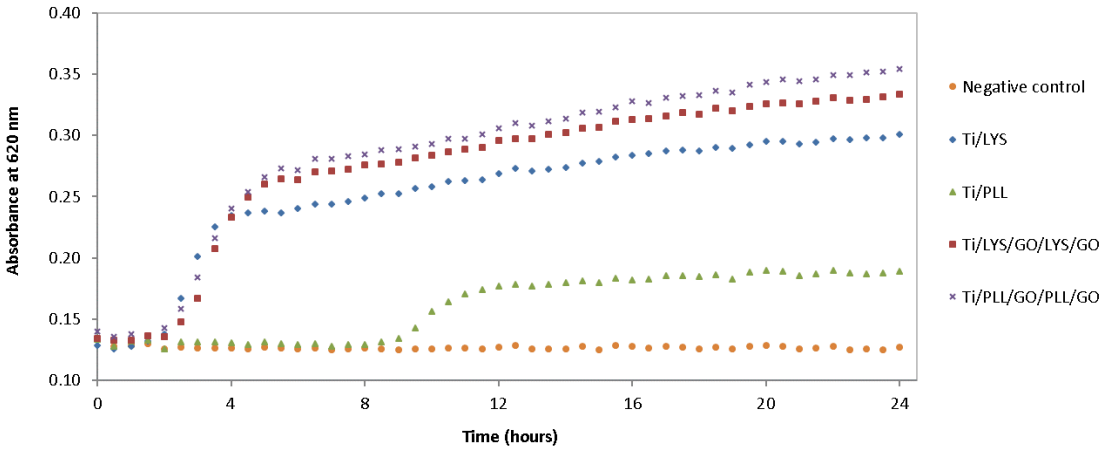

Figure 25. Results for the antimicrobial test of the coated-Ti surfaces.
Growth curves of *E. coli* at 37 °C over 24 h. Negative control: LB medium. Ti/LYS: *E. coli* growth in PBS buffer and LB medium on LYS-coated Ti substrate. Ti/PLL: *E. coli* growth in PBS buffer and LB medium on PLL-coated Ti substrate. Ti/LYS/GO/LYS/GO: *E. coli* growth in PBS buffer and LB medium on LYS/GO/LYS/GO-coated Ti substrate. Ti/PLL/GO/PLL/GO: *E. coli* growth in PBS buffer and LB medium on PLL/GO/PLL/GO-coated Ti substrate. Samples were prepared in triplicate and the average values are presented.

Finally, for the Ti/PLL/GO/PLL/GO sample, no inhibition of bacterial growth was observed and it was inclusively the tested surface that favored *E. coli* growth the most. Although several studied have demonstrated the strong antimicrobial activity of GO against a wide variety of microorganisms, including Gram-positive and gram-negative bacteria, the relationship between GO physicochemical properties and its antimicrobial activity that has yet to be elucidated. GO sheet size was found to influence its antimicrobial activity in suspension due to the capacity of larger sheets to completely wrap around the cells and isolate them from their environment (Perreault *et al.*, 2015). However, in the present case, GO sheets are immobilized in the PLL-coated Ti substrate, which means that the interactions between GO and the bacterial cells may be significantly different than in suspension. GO antimicrobial activity has been also attributed to oxidative mechanisms mediated by the higher defect density of smaller GO sheets. For example, Perreault and co-workers reported 4-fold increased antimicrobial activity of a GO-coated surface when the GO sheet size varied from 0.8 µm to 0.1 µm. By the SEM image obtained from the purified version of the GO dispersion used in this work (Fig. 10) the average sheet size tends to be over 10 µm. For this reason, it is possible that the GO sheets adsorbed to the PLL/GO/PLL/GO-coated Ti surface were not small enough to induce a significant oxidative stress on the surrounding bacteria and consequent cell death.

Ti is generally accepted has a biocompatible material, owning its already well stablished biomedical applications, namely for medical implant devices (Brunette *et al.*, 2001). The biocompatibility of equivalent Ti-coated samples was tested by direct contact with mouse connective tissue fibroblasts, cell line *L929* (DSMZ ACC 2), over 24 h. The cells viability was evaluated via the colorimetric WST-1 assay. Absorbance was measured at 450 nm and the relative percentage to the untreated control (bare Ti substrate) was calculated and is presented in Fig. 26.

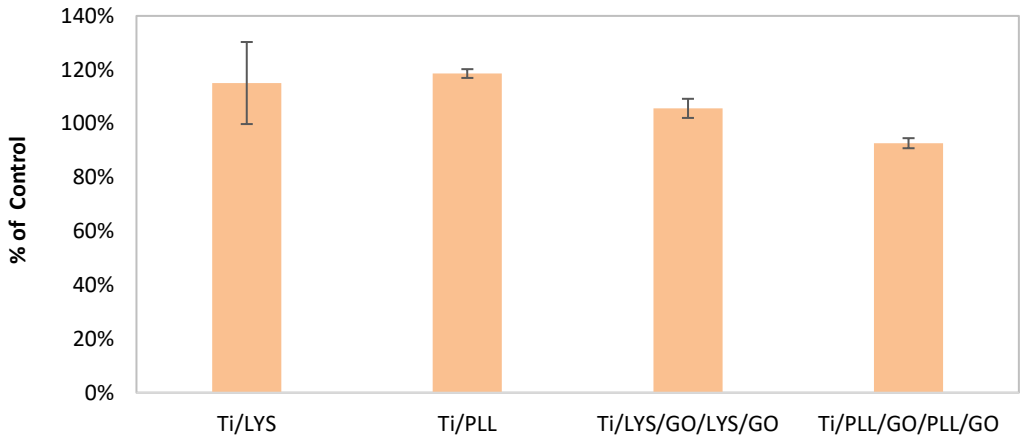

Figure 26. Results for the biocompatibility test of the coated-Ti surfaces.
Relative % to the control ± standard deviation of the measured absorbance at 450 nm. Samples were prepared in triplicate. The absorbance was measured after 24 h of contact between the mouse connective tissue fibroblasts (cell line *L929*) and the LYS-, PLL-, LAY/GO/LYS/GO- and PLL/GO/PLL/GO-coated Ti 6Al4V ELI surfaces.

For the Ti/LYS and Ti/PLL samples, values of 115 ± 15% and 119 ± 2% were found, revealing the remarkable biocompatibility of the LYS- and PLL-coated Ti substrates. The Ti/LYS sample presented a

relatively high standard deviation, but even the lowest possible value corresponded to approximately 100%. This was an expected result taking into account the already mentioned nature of the tested interfactants. Moreover, PLL has been widely used for biomedical applications, including as surface coating for promoting cell adhesion (Choi *et al.*, 2015). Concerning the Ti/LYS/GO/LYS/GO sample, a cell viability of approximately 106 ± 4% of the control was obtained. This value was once again very similar to the control, which seems to indicate that GO exposure promotes LYS desorption from the Ti substrate. On the other hand, PLL/GO/PLL/GO-coated Ti showed a decrease of 26% compared to the Ti/PLL sample. This is indication that the GO coating presented a lower biocompatibility than the PLL coating. Nevertheless, it is generally accepted that a sample is non-cytotoxic if the percentage of viable cell is equal to or greater than 70% of the untreated control (Ratner *et al.*, 2004). In fact, the percentage of viable cells after contact with Ti/PLL/GO/PLL/GO was approximately 93 ± 2% of the untreated control, which means that the GO-coated surface could be classified as non-cytotoxic.

Although a number of studies have been published on the potential toxicity of graphene materials, many discrepancies between the results remain. When considering GO biocompatibility, its intrinsic physicochemical properties, as well as differences in size dimensions, functionalization and purification may be considered, since these factors will always affect its toxicity to biological systems (Gurunathan and Kim, 2016). By the SEM images shown by Fig. 24, GO of variable size dimensions (average size over 10 μm) tended to form smooth layers on the PLL-coated solid surface. Additionally, by the antimicrobial test, the tested coating did not reveal potential for oxidative stress generation, which may also contribute for its biocompatible properties. In this specific case, PLL directed GO layer formation on Ti substrates and the good viability of the mouse connective tissue fibroblasts after 24 hours of contact with the functionalized surface revealed no cytotoxic effects.

CHAPTER 5

Conclusions

5.1 Main Findings and Accomplished Goals

Adsorption of a cationic and an anionic surfactant was tested on SiO_2 and TiO_2 solid surfaces. Under pH 4.7, CTAB considerably adsorbed on SiO_2 and TiO_2, which in the first case was attributed to electrostatic attractions between the cationic surfactant and the oxide surface. In the second case, it was mainly attributed to interactions of hydrophobic nature between the hydrocarbon chains of the surfactant molecules that could bind to the few negative sites on the TiO_2 surface. However, these interactions were not stable upon rinsing, resulting in a non-promising approach for GO layer formation on these solid surfaces. Regarding the anionic SDS, there was no interaction with SiO_2 surface due to electrostatic repulsion between both negatively charged molecules and solid surface. A considerable interaction between SDS and the TiO_2 was found to be very stable upon rinsing. This finding was related to specific adsorption of SO_4^{2-} ions on TiO_2, which would be consistent with a ligand exchange mechanism of adsorption for SDS on TiO_2.

Among the tested interfactants, PLL was identified as the most promising biomolecules upon directing GO layer formation on SiO_2 and TiO_2 substrates. By the QCM-D results, the polypeptide adsorption on solid surfaces is higher under pH conditions close to its IEP. Under both pH 6.1 and pH 9.0, there was clear formation of a GO layers on the top of the PLL-coated surfaces. It was also possible to conclude that PLL presents a very thin but compact adsorption on the tested oxide surfaces. On the other hand, PLL adsorption on the top of a pre-formed GO layer tends to exhibit a viscoelastic behavior, which is characteristic of a 'soft' adsorbed material. Consequently, QCM-D experiments tended to overestimate the amount of PLL adsorbed on the top of a GO-coated surface. These results were successfully confirmed by the XPS investigations when estimating the thickness evolution of analogue surfaces, coated by LbL assembly of PLL and GO. Based on the attenuation of the Si2p and Ti2p signals, there was indication of increasing thickness within the growing films. Additionally, by the XPS results it was clear that GO adsorption on the PLL-coated surfaces was favored under pH 6.1, bellow the IEP of the polypeptide. The substrate was found to influence the adsorption process in a way that growing films tend to be thicker on TiO_2 rather than on SiO_2.

When absorbed to a Ti surface, LYS showed to lose its characteristic antimicrobial properties, probably due to conformational changes. On the other hand, PLL-coated Ti surfaces induced a retarded growth of *E. coli* with a difference of 9 h comparing to the untreated control. Also, the maximum growth was three times lower than the untreated control in the stationary phase. Regarding the LYS/GO/LYS/GO coated Ti surfaces, there was a slightly higher *E. coli* growth compared to the LYS-coated surfaces, which might be an indication that there was no adsorption of GO on the top of the LYS-coated surface. Finally,

PLL/GO/PLL/GO-coated Ti surface showed no antimicrobial activity against *E. coli*. This fact could be related to the use of large-sized GO material, with an average size over 10 nm.

Biocompatibility properties of analogous surfaces were tested upon contact with mouse connective tissue fibroblasts (cell line *L929*). All surfaces showed remarkable biocompatibility. On the PLL/GO/PLL/GO-coated Ti surface there was 93% of cell viability compared to the untreated control. This finding may indicate the non-cytotoxic effect of GO-coated surfaces when GO layers are adsorbed on the top a PLL-coated substrate.

5.2 Additional Research

Additional QCM-D investigations focused on the interactions between a specific LAC formulation (laccase from *Trametes versicolor*, > 0.5 U/mg, Sigma-Aldrich, Germany) and GO were performed by the LbL assembly of this molecules on different substrates. The first findings were very clear, indicating formation of a GO layer on the top of the LAC-coated substrates. However, this system was restricted to the formation of a single GO layer, with no prospects for LbL assembly between these molecules.

Maltodextrins (*i.e.*, water soluble mixtures of carbohydrates) are often applied for lyophilization of proteins for protection from inactivation during freeze-drying (Ureña[1] *et al.*, 2016). Based on the possibility of presence of maltodextrin within the used commercial laccase formulation, QCM-D investigations were performed involving maltodextrin upon directing GO layer formation on different substrates. However, when a LAC formulation of higher activity (laccase C from *Trametes versicolor*, > 1 U/mg, ASA Spezialenzyme, Germany) was tested, no clear potential upon directing GO layer formation was revealed, as suggested by the presented QCM-D results in this work (chapter 4, sub-chapter 4.4.1). Thus, aqueous LAC-maltodextrin mixture suspensions of increasing maltodextrin concentration were prepared containing the LAC formulation of higher activity (> 1 U/mg) and pure maltodextrin. Its adsorption followed by GO was studied on different substrate surfaces by QCM-D and no prospects for LbL assembly between these molecules was revealed.

As for PLL, also XPS investigations were performed using LAC and LYS as interfactants upon directing GO layer formation on SiO_2 and TiO_2 substrates. Since the use of PLL revealed the most promising results under the tested conditions, only these investigations were presented in this work.

5.3 Limitations and Future Work

The QCM-D technology is a real-time surface sensitive technique, whose excellent performance is strongly dependent on the quality of the used quartz crystal sensors. These sensors are the substrate on which all the adsorption, desorption, molecular interactions and structural properties of thin films will be monitored and characterized. Stable, reliable and reproducible data is only guaranteed for one-time use of the sensors according to the supplier recommendations. Considering the high number of performed experiments throughout the course of this study, the use of one sensor per measurement would not be economically

viable. For this reason, SiO_2- and Ti-coated sensors were used multiple times, which did not allow presentation of reproducible data for the QCM-D measurements discussed in sections 4.3 and 4.4.

The fact that GO is a very large molecule (micrometer-sized) had a strong impact on the QCM-D operation. The material was continuously accumulating all over the tubing and QCM-D modules, which could promote contamination of the diverse injected solutions and variations in the settled flow rate. For this reason, the cleaning frequency of the QCM-D modules and tubing was considerably increased, which turned the cleaning procedures into a very time-consuming task.

Since both LAC and LYS proteins showed no clear interaction with GO by QCM-D technique, the used of rGO instead of GO would be an interesting way of characterizing the interaction between these biomolecules and graphene materials. rGO has a very reduced number of oxygen-containing groups which means that its interactions with LAC and LYS would be mainly attributed to van der Waals forces and hydrophobic interactions, decreasing the possibility of an electrostatic adsorption mechanism. Additionally, it would be interesting to test electrostatically inert, hydrophobic substrates for comparison with the obtained results for hydrophilic SiO_2 and TiO_2 substrates. In this case, the pH-induced net charge of the protein should have a minor effect on the protein-substrate interactions as compared with this case with charged surfaces. The different conformations assumed by the proteins on these surfaces could have a strong impact on its further interaction with GO, and the LbL assembly of these molecules could be more favored. As discussed before, variation of the pH within the LbL assembly process could also be an approach to be further explored for different interfactants since in the case of PLL, although its adsorption to the substrate was higher under pH close to its IEP, GO adsorption onto a PLL-coated surface showed to be favored under pH conditions below the IEP of the polypeptide. Finally, apart from the discussed factors influencing LbL assembly of biomolecules and GO, GO and interfactant concentrations, as well as ionic strength of the buffer should be assessed.

REFERENCES

Abergel DSL, Apalkov V, Berashevich J, Ziegler K, Chakraborty T. Properties of graphene: a theoretical perspective. *Advances in Physics*, 2010, 59:261-482.

Alwarappan S, Boyapalle S, Kumar A, Li CZ, Mohapatra S. Comparative study of single-, few, and multilayered graphene toward enzyme conjugation and electrochemical response. *Journal of Physical Chemistry C*, 2012, 116:6556-6559.

Ardley N. Kompaktwissen Physik & Chemie: [2000 Schlüsselbegriffe]. *Starnberg: Dorling Kindersley*, 2003.

Ariga K, Yamauchi Y, Rydzek G, Ji Q, Yonamine Y, Wu KCW, Hill JP. Layer-by-Layer nanoarchitectonics: Invention, innovation, and evolution. *Chemistry Letters CSJ*, 2014, 43:36-68.

Baweja L, Balamurugan K, Subramanian V, Dhawan A. Effect of graphene oxide on the conformational transitions of amyloid beta peptide: A molecular dynamics simulation study. *Journal of Molecular Graphics and Modelling*, 2015, 61:6556-6559.

Bertrand P, Jonas A, Laschewsky A, Legras R. Ultrathin polymer coatings by complexation of polyelectrolytes at interfaces: Suitable materials, structure and properties. *Macromolecular Rapid Communications*, 2000, 21:319−348.

Bertrand T, Jolivalt C, Briozo P, Caminade E, Joly N, Madzak C, Mougin C. Crystal structure of a four-copper laccase complexed with an arylamine: Insights into substrate recognition and correlation with kinetics. *ACS Biochemistry*, 2002, 41:7325-7333.

Bharech S, Kumar R. A Review on the properties and applications of graphene. *Journal of Material Science and Mechanical Engineering*, 2015, 2:70-73.

BiolinScientific. (1) "QCM-D Technology". Available: http://www.biolinscientific.com-/technology/qcm-d-technology/. Visited on 12 July 2017; (2) "Q-Sense Instruments". Available: http://www.biolinscientific.com/product/q-sense-analyzer/. Visited on 20 July 2017; (3) "Q-Sense Accessories". Available: http://www.biolinscientific.com/q-sense/products/. Visited on 20 July 2017; (4) "Q-Sense Sensor QSX 310 Ti". Available: http://www.biolinscientific.com/zafepress.php?url=%2Fextranet-new%2Fqsense%2FMarketing%20m-aterials%2FBrochures%20for%20printing%2FProduct%20Brochures%2FSensor%20spec%20sheet%20QSX310Ti.pdf. Visited on 16 August 2017.

Brunette DM, Tengvall P, Textor M, Thomsen P. Titanium in Medicine. *Springer*, 2001.

Cai B, Hu K Li C, Jin J Hu Y. Bovine serum albumin bioconjugated graphene oxide: Red blood cell adhesion and hemolysis studied by QCM-D. *Applied Surface Science*, 2015 356:844-851.

Chandra V, Kim KS. Highly selective adsorption of Hg2+ by polypyrrole-reduced graphene oxide composite. *Chemical Communications RSC*, 2011, 47:3942-3944.

Chandra V, Park J, Chun Y, Lee JW Hwang IC, Kim KS. Water dispersible magnetite-reduced graphene oxide composites for arsenic removal. *American Chemical Society Nano*, 2010, 4:3979-3986.

Chandrasekaran N, Dimartino S, Fee CJ. Study of the adsorption of proteins on stainless steel surfaces using QCM-D. *Chemical Engineering Research and Design*, 2013 91:1674-1683.

Choi JH, Kim SO, Linardy E, Dreaden EC, Zhdanov VP, Hammond PT, Cho NJ. Influence of pH and surface chemistry on poly(L-lysine) adsorption onto solid supports investigated by quartz crystal microbalance with dissipation monitoring. *Journal of Physical Chemistry B*, 2015, 19:10554-10565.

Chowdhury I, Duch MC, Mansukhani ND, Hersam MC, Bouchard D. Deposition and release of graphene oxide nanomaterials using a Quartz Crystal Microbalance. *Environmental Science and Technology ACS*, 2014, 48:961-969.

Chowdhury I, Hou WC, Goodwin D, Henderson M, Zepp RG, Bouchard D. Sunlight affects aggregation and deposition of graphene oxide in aquatic environment. *Water Research*, 2015, 78:37-46.

Coletti C, Riedl C, Lee DS, Krauss B, Patthey L, Klitzing K, Smet JH, Starke U. Charge neutrality and band-gap tuning of epitaxial graphene on SiC by molecular doping. *Physical Review B*, 2010, 81:235401.

Curie JP and Curie PCR. An oscillating quartz crystal mass detector. *Rendu*, 1880, 91:294-297.

Dreyer DR, Park S, Bielawski CW, Ruoff RS. The chemistry of graphene oxide. *Chemical Society Rewies*, 2010, 39:228-240.

Dubey N, Bentini R, Islam I, Cao T, Neto AHC, Rosa V. Graphene: A versatile carbon-based material for bone tissue engineering. *Stem Cells International*, 2015, 2015:804213.

Effah EA, Bianco PD, Ducheyne P. Crystal structure of the surface oxide layer on titanium and its changes arising from immersion. *Journal of Biomedical Materials Research*, 1995, 29:73-80.

Förch R, Schönherr H, Jenkins ATA. Surface Design: Applications in bioscience and nanotechnology. *Wiley-VCH Verlag GmbH*, 2009.

Gao W. Graphene Oxide: Reduction Recipes, Spectroscopy, and Applications. *Springer International Publishing*, 2012.

Gätjen, Linda. Provided by M.Sc. Linda Gätjen, 2017, Fraunhofer IFAM.

Georgakilas V, Tiwari JN, Kemp KC, Perman JA, Bourlinos AB, Kim KS, Zboril R. Noncovalent functionalization of graphene and graphene oxide for energy materials, biosensing, catalytic, and biomedical applications. *Chemical Reviews*, 2016, 116:5464-5519.

Georgalikas V, Otyepka M, Bourlinos AB, Chandra V, Kim N, Kemp KC, Hobza P, Zboril R, Kim KS. Functionalization of graphene: Covalent and non-covalent approaches, derivatives and applications. *Chemical Reviews*, 2012, 112:6156-6214.

Georgalikas V, Perman JA, Tucek J, Zboril R. Broad family of carbon nanoallotropes – clacification, chemistry and advanced architecture of fullerene, nanotube, graphene and their relatives. *Chemical Reviews*, 2015, 115:4744-4822.

Gou C, Book-Newell B, Irudayaraj J. Protein-directed reduction of graphene oxide and intracellular imaging. *Chemical Communications*, 2011, 47:12658-12660.

Graphenea, "Graphene oxide water dispersion". Available: https://www.graphenea.com/collections/graphene-oxide/products/graphene-oxide-4-mg-ml-water-dispersion-1000-ml. Visited on 26 August 2017.

Gurunathan S, Kim JH. Synthesis, toxicity, biocompatibility, and biomedical applications of graphene and graphene-related materials. *International Journal of Nanomedicine*, 2016, 11:1927-1945.

Haubner K, Murawski J, Olk P, Lukas M, Ziegler C, Adolphi B, Jaehne E. The route to functional graphene oxide, *ChemPhysChem*, 2010, 11:2131-2139.

Haubner K, Murawski J, Olk P, Lukas M, Ziegler C, Adolphi B, Jaehne E. The route to functional graphene oxide. *European Journal of Chemical Physics and Physical Chemistry*, 2010, 11:2131–2139.

Holmberg K. Novel Surfactants: Preparation Applications and Biodegradability, Second Edition, Revised and Expanded. *Marcel Dekker*, 2003.

Höök F, Rodahl M, Kasemo B, Brzezinski P. Structural changes in hemoglobin during adsorption to solid surfaces: Effects of pH, ionic strength, and ligand binding. *The National academy of Sciences*, 1998, 95:12271-12276.

Hummers WS, Offeman RE. Preparation of graphitic oxide. *Journal of the American Chemical Society*, 1859, 80:1339.

Hurt RH. All in the graphene family – A recommended nomenclature for two-dimensional carbon materials. *Carbon*, 2013, 65:1-6.

Hyldgaard M, Mygind T, Vad BS, Stenvang M, Otzen DE, Meyer RL. The Antimicrobial mechanism of action of epsilon-poly-L-lysine. *Applied and Environmental Biotechnology*, 2014, 80:7758-7770.

Jastrzębska AM, Kurtycz P, Olszyna AR. Recent advances in graphene family materials toxicity investigations. *Journal of Nanoparticle Research*, 2012, 14:1320.

Jordan CE, Frey BL, Kornguth S, Corn RM. Characterization of poly-L-lysine adsorption onto alkanethiol-modified gold surfaces with polarization-modulation Fourier transform infrared spectroscopy and surface plasmon resonance measurements. *Langmuir*, 1994, 10:3642:3648.

Karousis N, Sandanayaka ASD, Hasobe T, Economopoulos SP, Sarantopoulou E, Tagmatarchis N. Graphene oxide with covalently linked porphyrin antennae: Synthesis, characterization and photophysical properties. *Journal of Materials Chemistry*, 2011, 21:109-117.

Khoo X, Hamilton P, O'Toole GA, Snyder BD, Kenan DJ, Gristaff MW. Directed assembly of PEGylated-peptide coatings for infection-resistant titanium metal. *American Chemical Society*, 131:31.

Klinowski J, He H, Forster M, Lerf A. A new structural model for graphite oxide. *Chemical Physical Letters*, 1998, 287:53–56.

Kumar V, Srivastava S, Umrao S, Kumar, Nath G, Sumana G, Saxena PS, Srivastava A. Nanostructured palladium-reduced graphene oxide platform for high sensitive, label free detection of a cancer biomarker. *RSC Advances*, 2014, 4: 2267-2273.

Kundu N, Mukherjee D, Maiti TK, Sarkar N. Protein-guided formation of silver nanoclusters and their assembly with graphene oxide as an improved bioimaging agent with reduced toxicity. *Physical Chemistry Letters*, 2017, 8: 2291-2297.

Kwok DY, Neumann AW. Contact angle measurements and contact angle interpretation. *Advances in Colloid Interface Science*, 1999, 18:167-249.

Lalaoui N, David R, jamet H, Holzinger M, Goff AL, Cornier S. Hosting adamantane in the substrate pocket of laccase: Direct bioelectrocatalytic reduction of O2 on functionalized carbon nanotubes. *ACS Catalysis*, 2016, 6:4259-4264.

Li W, Wang F, Feng S, Wang J, Sun Z, Li B, Li Y, Yang J Elzatahry AA, Xia Y. Sol-gel design strategy for ultradispersed TiO2 nanoparticles on graphene for high-performance lithium ion batteries. *Journal of the American Chemical Society*, 2013, 135:18300-18303.

Lin Z. Evaporative self-assembly of ordered complex structures. *World Scientific Publishing*, 2012.

Liu Y, Dong X, Chen P. Biological and chemical sensors based on graphene materials. *Chemical Society Reviews*, 2012, 41:2283-2307.

Lu HC, Yang HH, Zhu CL, Chen X, Chen GN. A Graphene platform for sensing biomolecules. *Angewandte Chemie International Edition in English*, 2009, 48:4785-4787.

Lu JR, Su TJ, Thirtle PN, Thomas RK, Rennie AR, Cubitt R. The denaturation of lysozyme layers adsorbed at the hydrophobic solid/liquid surface studied by neutron reflection. *Journal Colloid and Interface Science*, 1998, 206:212–223.

Lu XK, Yu MF, Huang H, and Ruoff RS. Tailoring graphite with the goal of achieving single sheets**,** *Nanotechnology*, 1999, 10:269-272.

MacLeod JM, Rosei F. Molecular self-assembly on graphene. *Small*, 2014, 10:1038-49.

Madhavi V, Lele SS. Laccase: Properties and applications. *BioResources*, 2009, 4:1694-1717.

Mao H, Liang J, Zhang H, Pei Q, Liu D, Wu S, Zhang Y, Song XM. Poly(ionic liquids) functionalized polypyrrole/graphene oxide nanosheets for electrochemical sensor to detect dopamine in the presence of ascorbic acid. *Biosensors and Bioelectronics*, 2015, 70:289–298.

Matos CF, Galembeck F, Zarbin AJG. Multifunctional and environmentally friendly nanocomposites between natural rubber and graphene or graphene oxide. *Carbon*, 2014, 78:469-479.

Maynard DG. Sulfur in the environment. *Marcel Dekker*, 1998.

Meng W, Gall E, Ke F, Zeng Z, Kopchick B, Timsina R, Qiu X. Structure and interaction of graphene oxide–cetyltrimethylammonium bromide complexation. *Journal of Physical Chemistry C*, 2015, 119:21135-21140.

Mohamad NR, Marzuki NHC, Buang NA, Huyop F, Wahab RA. An overview of technologies for immobilization of enzymes and surface analysis techniques for immobilized enzymes. *Biotechnology and Biotechnological Equipment*, 2015, 205-220.

MyScope, "Principles of SEM operation". Available: http://www.ammrf.org.au/myscope/sem/practice/principles/. Visited on 9 September 2017.

Nanda SS, Yi1 DK, Kim K. Study of antibacterial mechanism of graphene oxide using Raman spectroscopy. *Nature Scientific Reports*, 2016, 6:28443.

Nobelprize.org, The Nobel Prize in Physics 2010, Available: http://www.nobelprize.org/nobel_prizes/physics/laureates/2010/.Visited on 8 June 2017.

Novoselov KS, Geim AK, Morozov SV, Jiang D, Zhang Y, Dubonos SV, Grigorieva IV, Firsov AA. Electric Field Effect in Atomically Thin Carbon Films. *Science*, 2004, 306:666-669.

Novoselov KS, Geim AK, Morozov SV, Jiang D, Zhang Y, Katsnelson MI, Grigorieva IV. Two-dimensional gas of massless Dirac fermions in graphene. *Nature*, 2005, 438:197-200.

Palanisamy S, Ramaraj SK, Chen SM, Velusamy V, Yang TCK, Chen TW. Voltammetric determination of catechol based on a glassy carbon electrode modified with a composite consisting of graphene oxide and polymelamine. *Microchimica Acta*, 2017, 184:1051–1057.

Pandey D, Reifenberger R, Piner R. Scanning probe microscopy study of exfoliated oxidized graphene sheets. *Surface Science*, 2008, 602:1607–1613.

Parks GA. The isoelectric points of solid oxides, solid hydroxides, and aqueous hydroxy complex systems. *Chemical Reviews*, 1965, 65:177-198.

Pei S, Cheng HM. The reduction of graphene oxide. *Carbon*, 2012, 50:3210-3228.

Perreault F, Faria AFF, Nejati S, Elimelech M. Antimicrobial properties of graphene oxide nanosheets: why size matters. *ACS Nano*, 2015, 9:7226-7236.

Petridis C, Savva K, Lin Y, Eda G, Kymakis E, Anthopoulos TD, Stratakis E. Post-fabrication, *in situ* laser reduction of graphene oxide devices. *Applied Physic Letters*, 2013, 102:093115.

Pires LB, López BP, Martinez CCM, Narváez EM, Domingo N, Esplandiu MJ, Alzina F, Torres CMS, Mercoçi A. Electrocatalytic tuning of biosensing response through electrostatic or hydrophobic enzyme–graphene oxide interactions. *Biosensors and Bioelectronics*, 2014, 61:655-662.

Porus M, Maroni P, Borkovek M. Response of adsorbed polyelectrolyte monolayers to changes in solution composition. *Langmuir*, 2012, 28:17506-17516.

PubChem, (1) "Polylysine". Available: https://pubchem.ncbi.nlm.nih.gov/compound/162282#section=Top. visited on 25 August 2017. Visited on 25 August 2017; (2) "L-lysine". Available: https://pubchem.ncbi.nlm.nih.gov/compound/5962#section=Top. Visited on 25 August 2017.

Q-Sense. Cleaning & Immobilization Protocols. Gothenburg, Sweden, Edition G, 2008.

Ratner BD, Hoffman AS, Schoen FJ, LemonsJE. Biomaterials science: An introduction to materials in medicine, 2004.

Richardson JJ, Cui J, Björmalm M, Braunger JA, Ejima H, Caruso F. Innovation in layer-by-layer assembly. *Chemical Reviews ACS*, 2016, 116:14828-14867.

Russell SR, Claridge SA. Peptide interfaces with graphene: an emerging intersection of analytical chemistry, theory, and materials. *Analytical Bioanalytical Chemistry*, 2016, 408:2649-2658.

Schmidt Th, Bauer E. Influence of interfactants on thin metals growth. *Surface Science*, 2001, 480:137-144.

Shih CJ, Lin S, Sharma R, Strano MS, Blankschtein D. Understanding the pH-dependent behavior of graphene oxide aqueous solutions: a comparative experimental and molecular dynamics simulation study. *Langmuir*, 2012, 28:235-241.

Simsikova M, Sikola T. Interaction off graphene oxide with proteins and applications of their conjugates. *Journal of nanomedicine Research*, 5:00109.

Simsikova M. Interaction of graphene oxide with albumins: Effect of size, pH, and temperature. *Archives of Biochemistry and Biophysics*, 2016, 593:69-79.

Stankovich S, Piner RD, Chen X, Wu N, Nguyen ST, Ruoff RS. Stable aqueous dispersions of graphitic nanoplatelets for the reduction of exfoliated graphite oxide in the presence of poly(sodium 4-styrenesulfonate). *Journal of Materials Chemistry*, 2006, 16:155-158.

Surwade SP, Smirnov SN, Vlassiouk SN, Unocic RR, Veith GM, Dai S, Mahurin SM. Water desalination using nanoporous single-layer graphene. *Nature Nanotechnology*, 2015, 10: 459-464.

Tang C, Long G, Hu X, Wong K, Lau WM, Fan M, Mei J, Xu T, Wang B, Huid D. Conductive polymer nanocomposites with hierarchical multi-scale structures *via* self-assembly of carbon-nanotubes on graphene on polymer-microspheres. *Nanoscale*, 2014, 6:7877-7888.

Tiwari JN, Kemp KC, Nath K, Tiwari RN, Nam HG, Kim KS. Interconnected Pt Nanodendrite/DNA/Reduced graphene oxide hybrid showing remarkable oxygen reduction activity and stability, *American Chemical Society Nano*, 2013, 7:9223-9231.

Ureña YRC, Cavalcanti WL Soltau M Villalobos K, Rischka K, Noeske PLM, Brune K Dieckhoff S. Interfactant action of an amphiphilic polymer upon directing graphene oxide layer formation on sapphire substrates. *Applied Adhesion Science*, 2017, 5:10.

Ureña1 YRC, Lisboa-Filho PN, Szardenings M, Gätjen L, Noeske PLM, Rischka K. Formation and composition of adsorbates on hydrophobic carbon surfaces from aqueous laccase-maltodextrin mixture suspensions. *Applied Surface Science*, 2016, 385:216-224

Ureña2 YRC, Gaetjen L, Nascimento MV, Filho PNL, Cavalcanti WL, Noeske PLM, Rischka K. Investigations of biofilms formed on silica in contact with aqueous formulations containing laccase and maltodextrin. *Applied Surface Science*, 2016, 4:2.

Vashist SK and Vashist P. Recent Advances in Quartz CrystalMicrobalance-Based Sensors. *Journal of Sensors*, 2011, Vol. 2011, Article ID: 571405.

Vertegel AA, Siegel RW, Dordick JS. Silica nanoparticle size influences the structure and enzymatic activity of adsorbed lysozyme. *Langmuir*, 2004, 20:6800–6807.

Wallace PR. The Band Theory of Graphite. *Physical Review*, 1947, 71:622-634.

Walsh RB, Wu B, Howard SC, Craig VSJ. Surface forces between titanium dioxide surfaces in the presence of cationic surfactant as a function of surfactant concentration, electrolyte concentration, and pH. *Langmuir*, 2014, 30:2789-2798.

Westwood M, Kirby AR, Parker R, Morris VJ. Combined QCM-D and AFM studies of lysozyme and poly-L-lysine-poly-galacturonic acid multilayers. *Carbohydrate Polymers*, 2012, 89:1222-1231.

Xu Y, Liu Z, Zhang X, Wang Y, Tian J, Huang Y, Ma Y, Zhang X, Chen Y. A graphene hybrid material covalently functionalized with porphyrin: synthesis and optical limiting property. *Advanced Materials*, 2009, 21:1275-1279.

Yang CS, Mahmood A, Kim B, Shin K, Jeon DH, Han JK, Bu SD, Park S, Choi WJ, Doudin B. Enhancing gas sensing properties of graphene by using a nanoporous substrate. *2D Materials*, 2016, 3:011007.

Yang, K, Chen B, Zhu L. Graphene-coated materials using silica particles as a framework for highly efficient removal of aromatic pollutants in water. *Nature Scientific Reports*, 2015, 5:11641.

Young T. An Essay on the Cohesion of Fluids. *Philosophical transactions of the Royal Society of London*, 1805, 95:65–87.

Yu L, Cheng C, Ran Q, Schlaich C, Noeske PLM, Li W, Wei Q, Haag R. Bioinspired universal monolayer combination concepts from blood protein adsorption and mussel adhesion. *ACS Applied Materials and Interfaces*, 2017, 9:6624-6633.

Zhang F, Zheng B, Zhang J, Huang X, Liu H, Guo S, Zhang J. Horseradish peroxidase immobilized on graphene oxide: Physical properties and applications in phenolic compound removal. *The Journal of Physical Chemistry C*, 2010, 114:8469-8473.

Zhang M, Naik RR, Dai L. Carbon Nanomaterials for Biomedical Applications, *Springer*, 2016.

Zhang QI, Wu Z, Li N, Pu Y, Wang B, Zhang T, Tao J. Advanced review of graphene-based nanomaterials in drug delivery systems: Synthesis, modification, toxicity and application. *Materials Science and Engineering: C*, 2017, 77: 1363–1375.

Zhang YB, Tan YW, Stormer HL, Kim P. Experimental observation of the quantum Hall effect and Berry's phase in graphene. *Nature*, 2005, 438:201-204.

Zhao J, Pei S, Ren W, Gao L, Cheng H-M. Efficient preparation of large-area graphene oxide sheets for transparent conductive films. *ACS Nano*, 2010, 4:5245–5252.

APPENDIX

A – Figures

A-Figure 1: Viscoelastic modeling of the adsorbed mass for the adsorption of SDS and CTAB followed by GO on SiO_2 and TiO_2 substrates by QCM-D.
Measurements were modeled applying the Q-sense Dfind model (Q-Sense, Gothenburg, Sweden) indicate in the table with a given model fit (%).

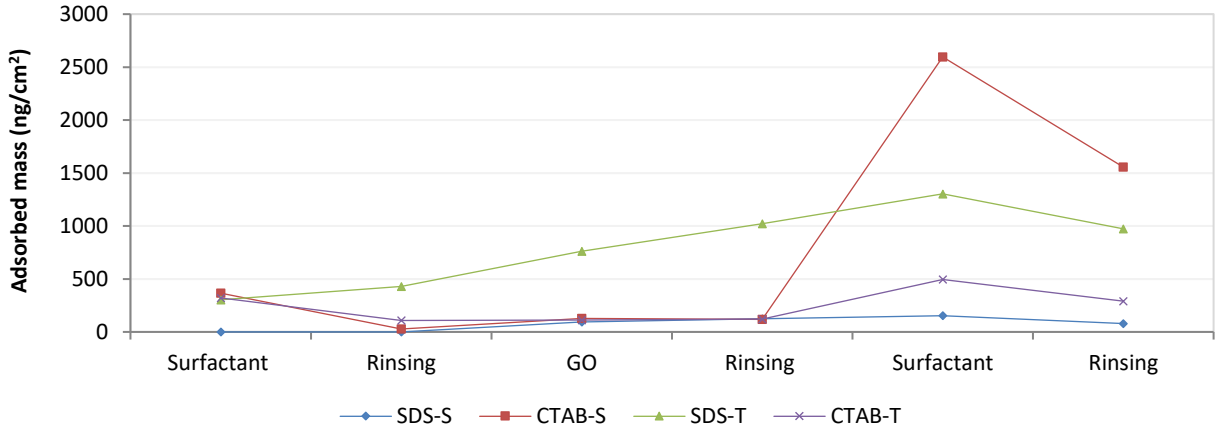

A–Figure 2: Viscoelastic modeling of adsorbed mass for the adsorption of LAC, LYS and PLL followed by GO on SiO_2 and TiO_2 substrates by QCM-D.
Measurements were modeled applying the Q-sense Dfind model (Q-Sense, Gothenburg, Sweden) indicate in the table with a given model fit (%).

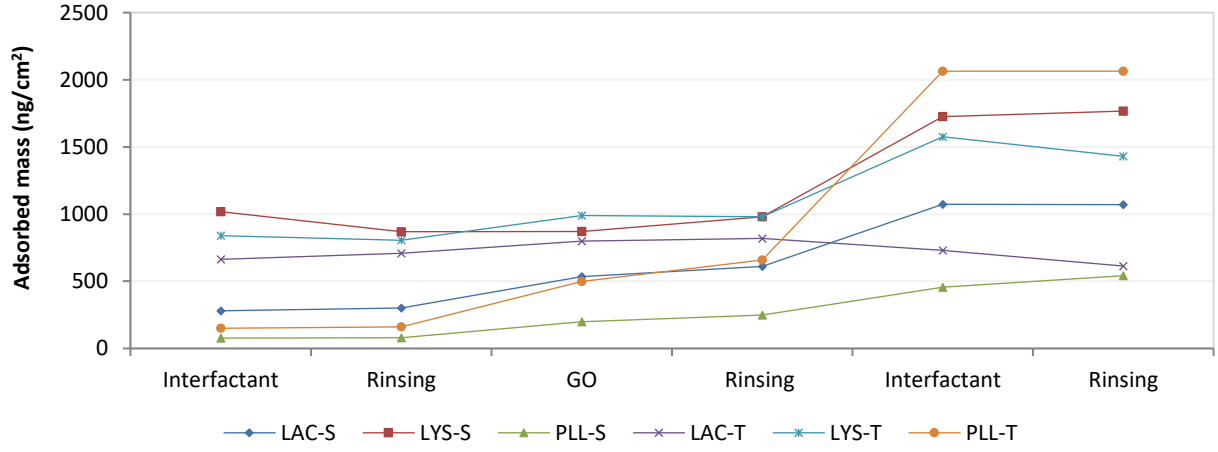

B – Tables

B–Table 1: Viscoelastic modeling of the thickness for the adsorption of SDS and CTAB followed by GO on SiO_2 and TiO_2 substrates by QCM-D.
Measurements were modeled applying the Q-sense Dfind model (Q-Sense, Gothenburg, Sweden) indicate in the table with a given model fit (%).

Measurement Label	Layer Thickness (nm)						Dfind Smart Fit Model
	Surfactant	Rinsing	GO	Rinsing	Surfactant	Rinsing	Model Fit
SDS-S	0.0	0.0	0.4	0.5	0.6	0.3	63%
CTAB-S	1.4	0.1	0.5	0.4	9.8	5.9	83%
SDS-T	0.7	1.0	1.8	2.4	3.1	2.3	100%
CTAB-T	0.8	0.3	0.3	0.3	1.2	0.7	54%

B–Table 2: Viscoelastic modeling of the thickness for the adsorption of LAC, LYS and PLL followed by GO on SiO_2 and TiO_2 substrates by QCM-D.
Measurements were modeled applying the Q-sense Dfind model (Q-Sense, Gothenburg, Sweden) indicate in the table with a given model fit (%).

Measurement Label	Layer Thickness (nm)						Dfind Smart Fit Model
	Interfactant	Rinsing	GO	Rinsing	Interfactant	Rinsing	Model Fit
LAC-S	1.1	1.1	2.0	2.3	4.1	4.0	83%
LYS-S	3.8	3.3	3.3	3.7	6.5	6.7	99%
PLL-S	0.3	0.3	0.8	0.9	1.7	2.0	91%
LAC-T	1.6	1.7	1.9	1.9	1.7	1.5	40%
LYS-T	2.0	1.9	2.1	2.3	3.7	3.4	99%
PLL-T	0.4	0.4	1.2	1.5	4.8	4.8	98

B–Table 3: Viscoelastic modeling of the thickness for the LbL assembly of LAC and GO on SiO_2 and TiO_2 substrates by QCM-D.
Measurements were modeled applying the Q-sense Dfind model (Q-Sense, Gothenburg, Sweden) indicate in the table with a given model fit (%).

Measurement Label	Layer Thickness (nm)										Dfind Smart Fit Model
	LAC	R*	GO	R	LAC	R	GO	R	LAC	R	Model Fit
LAC-GO-4.7S	1.4	1.4	1.5	1.5	1.7	2.0	2.6	3.4	4.3	4.2	85%
LAC-GO-4.7T	2.2	2.2	3.2	3.5	4.8	5.3	6.4	6.9	7.6	7.3	100%
LAC-GO-3.6S	1.2	1.1	1.1	1.1	1.4	1.3	1.3	1.3	1.4	1.4	88%
LAC-GO-3.6T	2.1	1.7	1.7	1.8	2.1	2.2	2.0	2.4	2.5	2.4	82%

*Rinsing

B–Table 4: Viscoelastic modeling of the thickness for the LbL assembly of LYS and GO on SiO_2 and TiO_2 substrates by QCM-D.

Measurements were modeled applying the Q-sense Dfind model (Q-Sense, Gothenburg, Sweden) indicate in the table with a given model fit (%).

Measurement Label	Layer Thickness (nm)										Dfind Smart Fit Model
	LYS	R*	GO	R	LYS	R	GO	R	LYS	R	Model Fit
LYS-GO-11S	2.4	2.3	2.4	2.5	3.0	2.7	2.7	2.6	3.1	2.6	91%
LYS-GO-11T	2.1	2.1	2.2	2.2	3.8	2.8	3.0	3.2	4.8	4.6	100%
LYS-GO-6.1S	3.1	3.2	3.6	3.7	4.9	4.9	5.0	5.1	6.4	6.3	99%
LYS-GO-6.1T	3.2	2.9	4.9	5.0	6.9	6.8	6.4	6.4	8.1	7.7	60%

*Rinsing

B–Table 5: Viscoelastic modeling of the thickness (nm) for the LbL assembly of PLL and GO on SiO_2 and TiO_2 substrates by QCM-D.

Measurements were modeled applying the Q-sense Dfind model (Q-Sense, Gothenburg, Sweden) indicate in the table with a given model fit (%).

	Layer Thickness (nm)										Dfind Smart Fit Model
Measurement Label	LYS	R*	GO	R	LYS	R	GO	R	LYS	R	Model Fit
PLL-GO-9S	0.4	0.4	1.1	1.4	2.0	2.0	4.0	5.1	6.6	6.2	91%
PLL -GO-9T	0.5	0.5	1.0	1.1	4.5	3.5	4.8	6.7	9.7	8.8	90%
PLL -GO-6.1S	0.2	0.2	0.5	0.5	1.6	1.7	2.1	2.3	2.8	2.9	98%
PLL -GO-6.1T	0.3	0.3	0.9	1.1	1.4	1.6	1.8	1.7	1.9	1.8	95%

*Rinsing

B-Table 6: Standard deviations (σ) of the XPS investigations for the coated SiO_2 surfaces.

Two positions for each sample were investigated. Standard deviations are given in at.%.

Sample	[Si] (at.%)	[O] (at.%)	[C] (at.%)	[N] (at.%)
Pristine SiO_2	0.0	0.8	0.8	0.0
S/PLL-9	0.12	0.19	0.07	0.01
S/PLL/GO-9	0.37	0.47	0.93	0.04
S/PLL/GO/PLL-9	0.28	0.35	0.69	0.07
S/PLL/GO/PLL/GO-9	0.37	0.57	0.93	0.03

Sample	[Si] (at.%)	[O] (at.%)	[C] (at.%)	[N] (at.%)
Pristine SiO_2	0.0	0.8	0.8	0.0
S/PLL-6.1	0.2	1.1	1.2	0.1
S/PLL/GO-6.1	0.8	1.4	2.1	0.1
S/PLL/GO/PLL-6.1	0.2	0.1	0.3	0.1
S/PLL/GO/PLL/GO-6.1	1.4	1.6	2.9	0.1

B-Table 7: Standard deviations (σ) of the XPS investigations for the coated TiO_2 surfaces.

Two positions for each sample were investigated. Standard deviations are given in at.%.

Sample	[Ti] (at.%)	[O] (at.%)	[C] (at.%)	[N] (at.%)
Pristine TiO_2	0.4	0.2	0.0	0.0
T/PLL-9	0.5	0.3	0.8	0.1
T/PLL/GO-9	0.7	0.7	1.6	0.0
T/PLL/GO/PLL-9	0.4	0.3	0.5	0.1
T/PLL/GO/PLL/GO-9	0.1	0.1	0.4	0.1

Sample	[Ti] (at.%)	[O] (at.%)	[C] (at.%)	[N] (at.%)
Pristine TiO_2	0.4	0.2	0.0	0.0
T/PLL-6.1	0.2	0.1	0.0	0.0
T/PLL/GO-6.1	0.1	0.3	0.7	0.2
T/PLL/GO/PLL-6.1	0.1	0.4	0.6	0.2
T/PLL/GO/PLL/GO-6.1	1.2	1.3	2.7	0.1

C – Further Information

C-1: Calculations for buffer preparations

Sodium Acetate Buffer

Molar mass (Sodium Acetate) = 82.03 g/mol

Molar mass (Acetic Acid) = 60.05 g/mol

ρ (Acetic Acid) = 1.05 g/mL

Volume of Acetic Acid (99.7%) to prepare 1000 mL of 200 mM Acetic Acid solution

$60.05\ \text{g/mol} \times 0.2\ \text{mol} \times 1/1.05\ \text{mL/g} \times 100.3\% = 11.78\ \text{mL}$ Acetic Acid

Mass of Sodium Acetate (99%) to prepare 1000 mL of 200 mM Sodium Acetate solution

$82.03\ \text{g/mol} \times 0.2\ \text{mol} \times 101\% = 16.57\ \text{g}$ Sodium Acetate

MES Buffer

Molar mass (MES) = 195.24 g/mol

Mass of MES (99.5%) to prepare 250 mL of 30 mM MES solution

$195.24\ \text{g/mol} \times 0.03\ \text{mol} \times 0.25\ \text{L} \times 100.5\% = 1.47\ \text{g}$ MES

C-2: Calculations for SDS and CTAB molar concentration

$$\text{Molar mass (SDS)} = 288.4\,\frac{\text{g}}{\text{mol}}$$

$$0.1\ \frac{\text{mg}}{\text{mL}} \times \frac{1}{288.4 \times 10^3}\,\frac{\text{mol}}{\text{mg}} = 3.47 \times 10^{-4}\ \text{M} = 0.35\ \text{mM}$$

$$\text{Molar mass (CTAB)} = 364.5\,\frac{\text{g}}{\text{mol}}$$

$$0.1\ \frac{\text{mg}}{\text{mL}} \times \frac{1}{364.5 \times 10^3}\,\frac{\text{mol}}{\text{mg}} = 2.74 \times 10^{-4}\ \text{M} = 0.27\ \text{mM}$$